Chapter 1: Introduction

1.1 General Introduction

Energy supply has arguably become one of the most important problems facing humanity. The exponential demand for energy is evidenced by dwindling fossil fuel supplies and record-high oil and gas prices due to global population growth and economic development (Figure 1-1). This energy shortage has significant implications to the future of our society—for example, in order for 10 billion people to sustain their current lifestyle with their current energy consumption, we need a minimum of ten additional terawatts (TWs), an equivalent of 150 millions of barrels of oil per day (150 M BOE/Day), until the year 2050 [1]. The energy crisis is further exacerbated by major concerns about global warming from greenhouse gas emissions due to increasing fossil fuel consumption [2, 3].

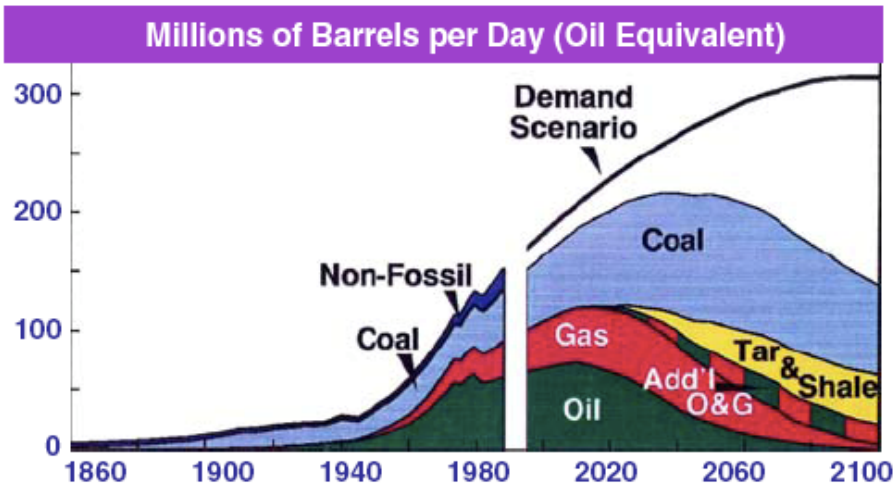

Figure 1-1 Historical and projected world energy supply and demand [4].

At this large scale, solar energy seems to be the most viable choice to meet our clean energy demand. The sun continuously delivers to the earth 120,000 TW of energy, which dramatically exceeds our current rate of energy needs (13 TW). This implies that covering only 0.1% of the earth's surface with solar cells of 10% efficiency would satisfy our current energy needs [4]; however, the energy currently produced from sunlight remains less than 0.1% of the global energy demand (Figure 1-2, data from [5]). The major barrier for the large-scale use of solar energy is the high cost and inadequate efficiencies of existing solar cells. Innovations are needed to harvest incident solar photons with greater efficiency and economical viability [6].

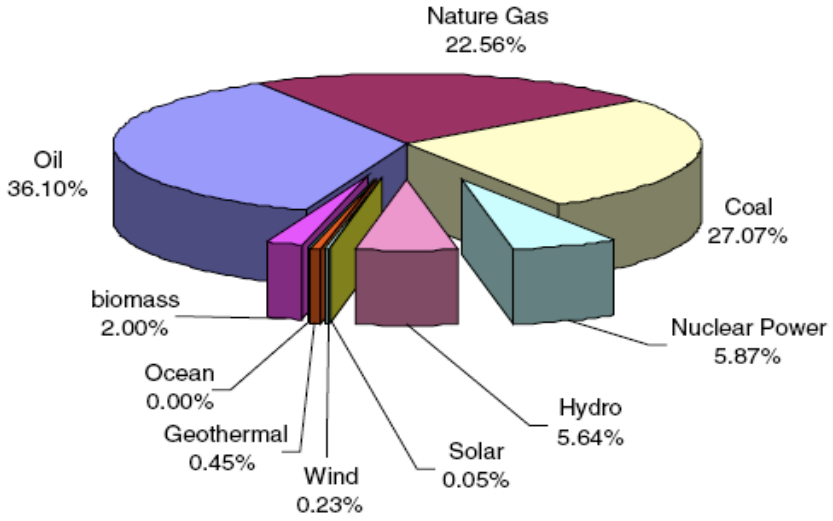

Figure 1-2 Worldwide primary energy consumption by energy type [11].

The best commercial solar cells based on single-crystal silicon are about 18% efficient [3]. These conventional p-n junction cells, so-called first-generation devices, suffer from the high cost of manufacturing and installation. The second-generation devices consisting of $CuInGaSe_2$ (CIGS) polycrystalline semiconductor thin films can reduce the price significantly, but it does not reduce the challenge to make their efficiencies more practical. Now the

third-generation solar cells, such as dye-sensitized solar cells (DSSCs) [7, 8], bulk heterojunction cells [9], and organic cells [10], are promising for inexpensive and large-scale solar energy conversion (Table 1-1 [3]).

	Laboratory best (%)	Thermodynamic limit (%)
Single junction		31
Silicon (crystalline)	25	
Silicon (nanocrystalline)	10	
Gallium arsenide	25	
Dye-sensitized	10	
Organic	5	
Multijunction	32	66
Concentrated sunlight (single junction)	28	41
Carrier multiplication		42

Table 1-1 Photovoltaic conversion efficiencies [3].

Nanostructured semiconductors, organic-inorganic hybrid assemblies, and molecular assemblies present new opportunities to design such third-generation light energy conversion devices. Considerable efforts have been devoted to the development of more efficient photoanode materials, such as ordered mesostructured materials [11] and one-dimensional (1-D) nanostructures (nanowires, nanotubes, and nanorods) [12-14]. Examples of 1-D nanostructures include highly ordered TiO_2 nanotube arrays synthesized with anodization of Ti foils, ZnO nanowire arrays synthesized with aqueous solutions, and carbon nanotube (CNT) and Si nanowire arrays synthesized with chemical vapor deposition (CVD) [13–24].

Bandgap-tunable semiconductor zero-dimensional (0-D) nanomaterials, such as CdS [25–27], PbS [28, 29], Bi_2S_3 [28, 30], CdSe [31], and InP [32] quantum dots (QDs), have demonstrated extraordinary optical and electronic properties that open up possibilities for revolutionary advances in photovoltaic (PV) devices. The combination of 1-D with 0-D nanostructures is attracting more interests from the solar cell community.

Of the materials being developed for photoelectrolysis applications, titania remains the most promising because of its high efficiency, low cost, chemical inertness, and photostability [36–38]. However, the widespread technological use of titania is impaired by its wide band gap (3.2 eV), which requires ultraviolet (UV) irradiation for photocatalytic activation. Because UV light accounts for only a small fraction (8%) of the sun's energy compared to visible light (45%), any shift in the optical response of titania from the UV towards full spectrum light will have a positive impact on the photocatalytic and photoelectrochemical utility of the material.

1.2 Dye-Sensitized Solar Cell

The sensitization of wide band gap semiconductors by adsorbed monolayers of dye molecules began in the late 1960s with the work of Gerischer and Memming [33]. A conceptual and practical breakthrough occurred in the late 1980s when Gratzel and co-workers started using high-surface-area semiconductors for dye-sensitized solar cells [34-37]. A sintered film of ~15 nm nanocrystalline TiO_2 particles, with an effective surface area ~1000 times higher than the geometrical area of the electrode, enabled a monolayer of sensitizing dye to absorb 99% of the incident sunlight at its absorption maximum. A concentrated redox electrolyte solution that permeated the TiO_2 film allowed the transfer of holes from the oxidized dye to the solution and ultimately to the counter electrode. The use of high surface area (nanoporous) substrates was quickly recognized as a major advance in dye-sensitization.

1.2.1 Construction

A DSSC consists of a nanocrystalline, mesoporous network of a wide band gap semiconductor (usually TiO_2), which is covered with a monolayer of dye molecules (usually a Ru dye). The semiconductor is deposited onto a transparent conductive oxide (TCO) electrode, through which the cell is illuminated. The TiO_2 pores are filled with a redox electrolyte (I^-/I_3^-) that acts as a conductor and that is electrically connected to a platinum electrode. The construction is illustrated as Figure 1-3.

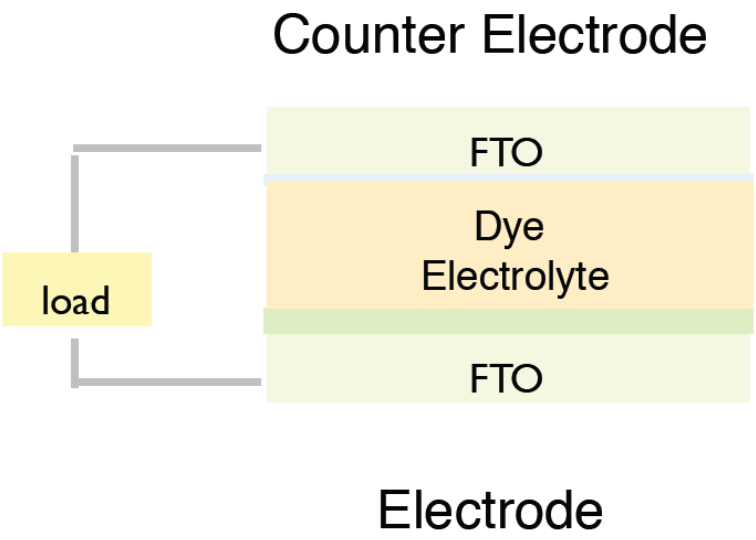

Figure 1-3 The construction of dye-sensitized solar cell.

TiO_2

At the heart of the system is a mesoscopic semiconductor oxide film. The material of choice has been TiO_2 (anatase), although alternative wide-band-gap oxides such as ZnO and Nb_2O_5 have also been investigated (Figure 1-4). Screenprintable TiO_2 pastes are used for the

manufacturing of small sized cells and masterplates. The colloids are synthesized following hydrothermal sol-gel procedures via either acidic or basic preparation procedures [35, 38]. Changing the synthesis conditions does influence primary particle sizes. Home-made TiO_2 colloids and commercial powders like P25 (Degussa) were transformed into screenprintable pastes, based on formulations containing terpineol and ethylcellulose as organic media binders.

Dye

Recent work has focused on the molecular engineering of suitable ruthenium compounds, which are known for their excellent stability. cis-Di-(thiocyanato)-bis(2,2´-bipyridyl)-4,4´-dicarboxylate) ruthenium-(II), coded as N3 or N719 dye depending on whether it contains four or two protons, was found to be an outstanding solar light absorber and charge-transfer sensitizer [39].

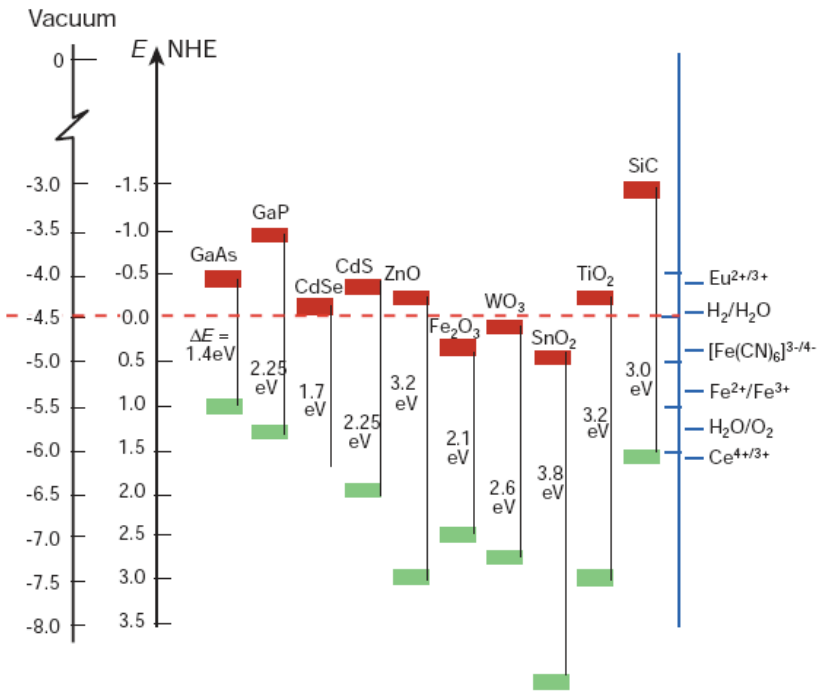

Figure 1-4 Band positions of several semiconductors in contact with aqueous electrolyte at pH 1. The lower edge of the conduction band (red colour) and upper edge of the valence band (green colour) are presented along with the band gap in electron volts. The energy scale is indicated in electron volts using either the normal hydrogen electrode (NHE) or the vacuum level as a reference. Note that the ordinate presents internal and not free energy. The free energy of an electron–hole pair is smaller than the band gap energy due to the translational entropy of the electrons and holes in the conduction and valence band, respectively. On the right side the standard potentials of several redox couples are presented against the standard hydrogen electrode potential.

The performance of this red ruthenium complex was for a long time unmatched by any other dyestuff. A few years ago, a black dye was discovered that shows a performance comparable to that of N3 as a charge-transfer sensitizer in the DSSC [19]. The structure of these sensitizers is shown in Figure 1-5. Recently, heteroleptic analogues to the N3 ruthenium

dye carrying only one carboxylated bipyridyl ligand have been introduced, with the other bipyridyl being modified by hydrophobic chains or extended π-conjugated systems. The IPCE is plotted as a function of the wavelength. The IPCE values exceed 80% in the wavelength range near the absorption maximum of the sensitizer, which is located around 530 nm. Taking into account the light losses from the absorption and reflection by the FTO glass, the conversion of photons that strike the TiO_2 film into electric current is almost quantitative. Even at 700 nm, where the absorption of light by the dye is weak, as shown in Figure 1-6, the IPCE value is still about 50%. Very high IPCEs can also be achieved with organic dyes. Such sensitizers that come close to matching the efficiency of the N-719 dye [40] have recently been developed in Japan [41].

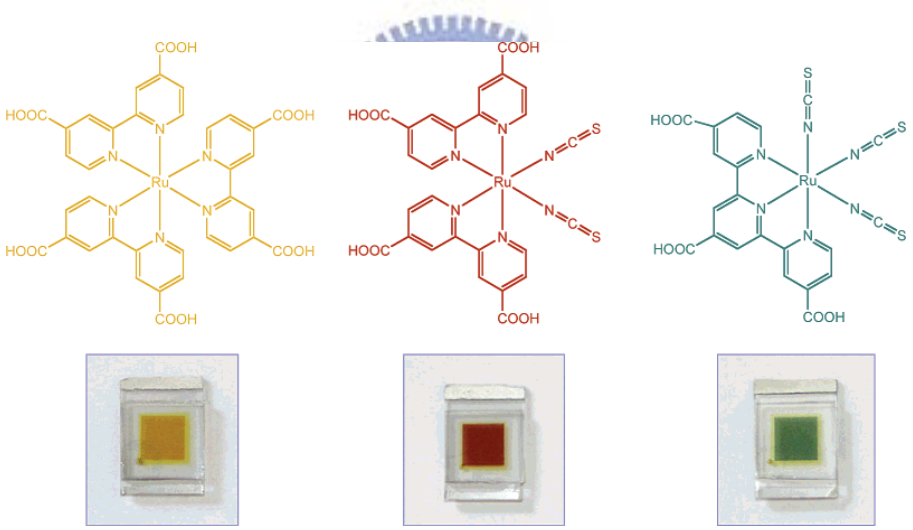

Figure 1-5 Structure of the ruthenium sensitizers RuL_3 (yellow) cis-$RuL_2(NCS)_2$ (red) and $RuL'(NCS)_3$ (green) where L = 2,2´-bipyridyl-4,4´-dicarboxylic acid and L´= 2,2´,2´´-terpyridyl-4,4,´4´´-tricarboxylic acid. The lower part of the picture shows nanocrystalline TiO_2 films loaded with a monolayer of the respective sensitizer. The film thickness is 5 µm.

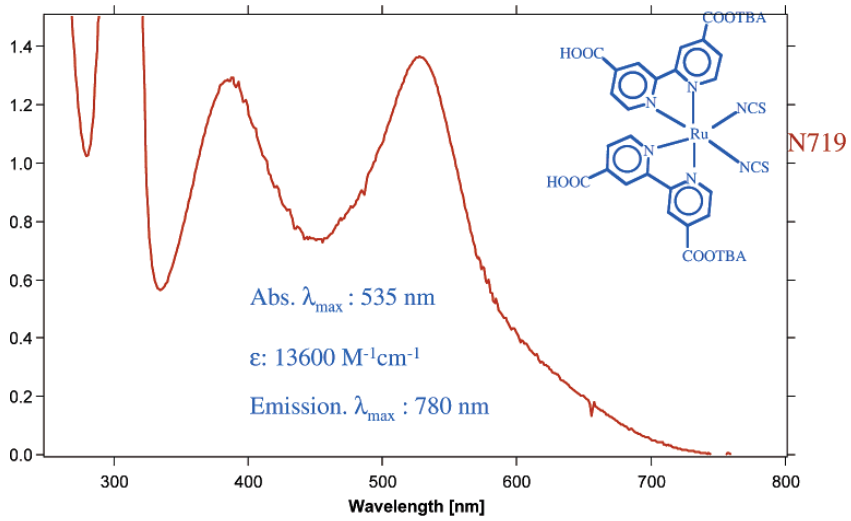

Figure 1-6 Absorption spectrum of the N719 dye in ethanol featuring two MLCT bands.

Electrolytes

The electrolyte mixtures used in high-efficiency cells mainly consist of alkylimidazolium iodides or tetra-alkyl ammoniumiodides, LiI, I_2 and surface additives such as tert-butylpyridin (TBP), benzimidazole derivatives like benzimidazole (BI) and N-Methylbenzimidazole (NMBI) in solvents such as acetonitrile, propionitrile or mixtures of acetonitrile and valeronitrile.

Counterelectrode

As the standard counterelectrode, SnO_2:F (FTO) substrates coated with a catalytic amount of platinum (Pt) are used. The standard counterelectrodes of the masterplates were obtained by screenprinting a Pt-based paste, after which a heat treatment at 450℃ is applied to obtain homogeneous layers of Pt on FTO. Another way to apply the Pt-layer is by solvent casting of an organic platinum precursor (H_2PtCl_6) containing solution and subsequent heat treatment at 450℃. Charge Transfer resistances (RCT) are <1 cm^2. An alternative method to manufacture Pt counter electrodes at low temperatures is investigated at CUTECH, resulting in a fine, nanoparticle sized layer of a selected metal on the support. In this method, called

POLYOL, a platinum salt (i.e., PtCl4 or K2PtCl6) is diluted in a mixture of organic solvents and by a reduction process carried out at temperatures ranging from 90 to 160℃, and Pt is precipitated directly on the supporting material. The advantage of this process is the formation of a fine, highly nanoparticulate sized layer of Pt on the substrate at a relatively low temperature. It has been shown that a reaction temperature of 90℃ is in principle enough to prepare counterelectrodes with a sufficiently low RCT to be applied in high efficiency DSSC. The lowest RCT found was around 0.5 cm^2.

1.2.2 Operational Principle of the DSSC

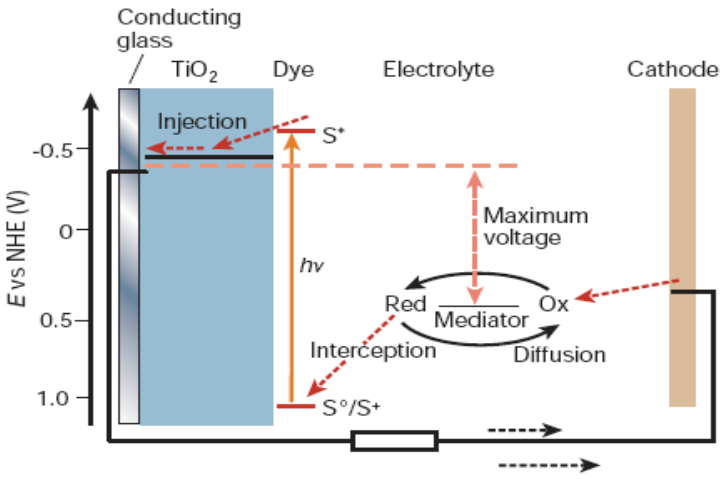

Figure 1-7 Schematic of operation of the dye-sensitized electrochemical photovoltaic cell. The photoanode, made of a mesoporous dye-sensitized semiconductor, receives electrons from the photo-excited dye which is thereby oxidized, and which in turn oxidizes the mediator, a redox species dissolved in the electrolyte. The mediator is regenerated by reduction at the cathode by the electrons circulated through the external circuit.

A schematic presentation of the operating principles of the DSSC is given in Figure 1-7. At the heart of the system is a mesoscopic semiconductor oxide film, which is placed in contact with a redox electrolyte or an organic hole conductor. Attached to the surface of the nanocrystalline film is a monolayer of the sensitizer. Photoexcitation of the latter results in the injection of an electron into the conduction band of the oxide. The dye is regenerated by electron donation from the electrolyte, usually an organic solvent containing a redox system, such as the iodide/ triiodide couple. The regeneration of the sensitizer by iodide intercepts the recapture of the conduction band electron by the oxidized dye. The iodide is regenerated, in turn, by the reduction of triiodide at the counter electrode, with the circuit being completed via electron migration through the external load. The voltage generated under illumination corresponds to the difference between the Fermi level of the electron in the solid and the redox potential of the electrolyte. Overall, the device generates electric power from light without suffering any permanent chemical transformation. The reactions are described as below:

1. Dye + light → Dye*

2. $Dye^* + TiO_2 \rightarrow e^-[TiO_2] + Dye^+$

3. $e^-[TiO_2] + C.E. \rightarrow TiO_2 + e^-[C.E.] + energy$

4. $1/2\ I_3^- + e^-[C.E.] \rightarrow 3/2\ I^- + C.E.$

1.2.3 Photovoltaic Performance

There are several important measures that are used to characterize solar cells. The most obvious is the total amount of electrical power produced for a given amount of solar power shining on the cell. Expressed as a percentage, this is known as the solar conversion efficiency. Electrical power is the product of current and voltage, so the maximum values for these measurements are important as well, J_{sc} and V_{oc} respectively. Finally, in order to understand the underlying physics, the IPCE (incident photon-to-electron conversion) is used to compare

the chance that one photon (of a particular energy) will create one electron. The maximum voltage generated by such a cell, in theory, is simply the difference between the (quasi-) Fermi level of the TiO_2 and the redox potential of the electrolyte, about 0.7 V under solar illumination conditions (V_{oc}). That is, if an illuminated DSSC is connected to a voltmeter in an "open circuit", it would read about 0.7 V. In terms of voltage, DSSC's offer slightly higher V_{oc} than silicon, about 0.7 V compared to 0.6 V. This is a fairly small difference, so real-world differences are dominated by current production, J_{sc}. Although the dye is highly efficient at turning absorbed photons into free electrons in the TiO_2, it is only those photons which are absorbed by the dye that ultimately result in current being produced. The rate of photon absorption depends upon the absorption spectrum of the sensitized TiO_2 layer and upon the solar flux spectrum. The overlap between these two spectra determines the maximum possible photocurrent. The efficiency is described in following equation:

$$\eta = \frac{P_{\text{out}}}{P_{\text{in}}} = \frac{J_{\text{sc}} \times V_{\text{oc}} \times \text{FF}}{P_{\text{in}}}$$

Another defining term in the overall behavior of a solar cell is the fill factor (FF). This is the ratio of the maximum power point divided by the open circuit voltage (V_{oc}) and the short circuit current (J_{sc}):

$$FF = \frac{P_m}{V_{oc} \times J_{\text{sc}}}$$

The fill factor is directly affected by the values of the cells series and shunt resistance. Increasing the shunt resistance (R_{sh}) and decreasing the series resistance (R_s) will lead to higher fill factor, thus resulting in greater efficiency, and pushing the cells output power closer towards its theoretical maximum.

Incident photon-to-electron conversion (IPCE) is the ratio of the number of charge carriers collected by the solar cell to the number of photons of a given energy shining on the solar cell. IPCE therefore relates to the response of a solar cell to the various wavelengths in

the spectrum of light shining on the cell. The IPCE is given as a function of either wavelength or energy, where Φ is the monochromatic light intensity:

$$\mathrm{IPCE}(\%) = \frac{1240(\mathrm{eV}\cdot\mathrm{nm}) \times J_{sc}\left(\frac{\mu\mathrm{A}}{\mathrm{cm}^2}\right)}{\lambda(\mathrm{nm}) \times \Phi\left(\frac{\mu\mathrm{W}}{\mathrm{cm}^2}\right)} \times 100$$

Chapter 2: Literatures Review

Considerable efforts have been devoted to the development of more efficient photoanode materials, such as ordered mesostructured materials [11] and one dimensional (1-D) nanostructures (nanowires, nanotubes, and nanorods) [12–14]. We investigate the effects of the electrode film morphology on the performance of a DSSC by reviewing cells based on different working electrodes structures, namely, nanopartical in section 2.1, nanowire in section 2.2, nanotube in section 2.3, nanotube combining AAO in section 2.4, and hollow sphere in section 2.5. We examine the effects of electrode structural uniformity and order on the charge carrier dynamics and thus on the injection, collection, and photoconversion efficiencies.

2.1 Nanopartical-Based DSSC

The first laboratory embodiment of the DSSC used a titanium sheet covered with a high surface-area "fractal" TiO_2 film that was produced by a sol-gel method. The roughness factor of the film was about 150. The open-circuit voltage of the cell was 1 V under illumination with a halogen spotlight. The device converted more than 60% of the incident photons to electric current at the absorption maximum of the sensitizer near 470 nm, and the overall conversion efficiency in full sunlight was between 1 and 2% [42]. Figure 2-1 shows the structure of the nanocrystalline semiconductor oxide electrode used today in the DSSC as an electron collector to support a molecular or QD sensitizer. The most widely used oxide material is TiO_2, although other wide-band semiconductor oxides such as ZnO, SnO_2, or Nb_2O_5 have also been employed. Nanoparticles of the oxide are deposited, for example, by screen printing onto a glass or flexible plastic support covered with a transparent conducting layer of fluorine-doped tin dioxide (FTO) or tindoped indium oxide (ITO). Each particle is

coated with a monolayer of sensitizer or a QD formed by self-assembly from a staining solution.

Typically, the anatase nanoparticles are prepared with a hydrothermal method [43]. They exhibit predominantly a bi-pyramidal shape, with the exposed facets having (101) orientation, which is the lowest energy surface of anatase. Their average size is 20 nm. A short sintering process is usually applied to ensure that the particles are electronically interconnected. To enhance the light-harvesting capacity of the dye-sensitized film in the red or near-infrared region, larger anatase particles of 200-400 nm radiuses are either mixed in the film or printed as an overlayer on top of the smaller particles.

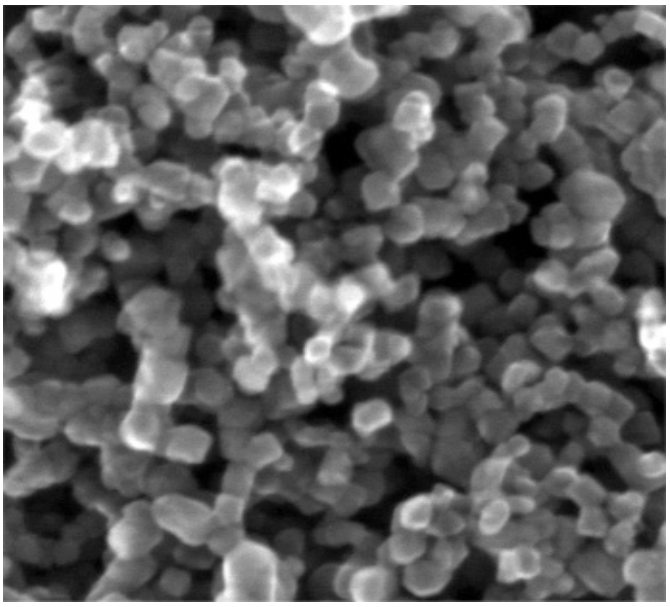

Figure 2-1 Scanning electron micrograph of a sintered mesoscopic TiO_2 film supported on an FTO glass. The exposed facets of the anatase nanocrystals are mainly oriented in the (101) direction. The average particle size is 20 nm.

2.2 Nanowire-Based DSSC

Although the high surface area of a nanoparticle film meets the requirement of adsorbing large amount of dyes in the monolayer, it brings about, at the same time, many opportunities for the recombination of photoinjected electrons and the oxidized dye and/or the electron acceptors in the electrolyte. However, the small size of the individual nanoparticles cannot support a space charge layer, which is essential for charge separation in bulk semiconductor [44]. 1-D nanostructures are promising for photovoltaic devices due to several performance and processing benefits, such as a direct path for charge transport and large surface areas for light harvest offered by the geometry of such nanostructures. Besides, the mobility of electrons in 1-D nanostructures is typically several orders of magnitude higher than that in semiconductor nanoparticle films commonly used in DSSCs (Table 2-1). Using a sufficiently dense array of long, thin nanowires as a dye scaffold, it should be possible to increase the DSSC dye loading (and so its absorption of red light) while simultaneously maintaining very efficient carrier collection. Law et al. [13] made ZnO nanowire arrays (Figure 2-2) of high surface area in aqueous solution using a seeded growth process [45] that was modified to yield long wires and showed that the injection process in nanowires is complete after ~5 ps, but continues for ~100 ps in the nanoparticles.

Nanomaterials	Electron mobilities (cm^2 V^{-1} s^{-1})
SWCNT	7.9^{a}–$10^{b} \times 10^{4}$
Si nanowire	1000^{c}
Ge nanowire	600–700^{d}
ZnO nanowire	1–5^{e}
ZnO nanoparticle film	0.017–0.066^{f}
TiO_2 nanoparticle film	$<10^{-3g}$

Table 2-1 Comparison of electron mobilities (cm^2 V^{-1} s^{-1}) of 1-D nanomaterials and nanoparticles. [a] Field-effect and; [b] intrinsic mobility of a 300 nm long and 3.9 nm diameter single-walled carbon nanotube (SWCNT); [c] 8–30 nm wide Si nanowires; [d] 20 nm wide Ge nanowires; [e] 16–17 μm long and 130–200 nm wide ZnO nanowire [46]; [f] for particle size around 4 nm [47]; [g] for 4–8 nm anatase TiO_2 nanocrystals; it is 15 cm^2 V^{-1} s^{-1} in single crystal TiO_2 [48].

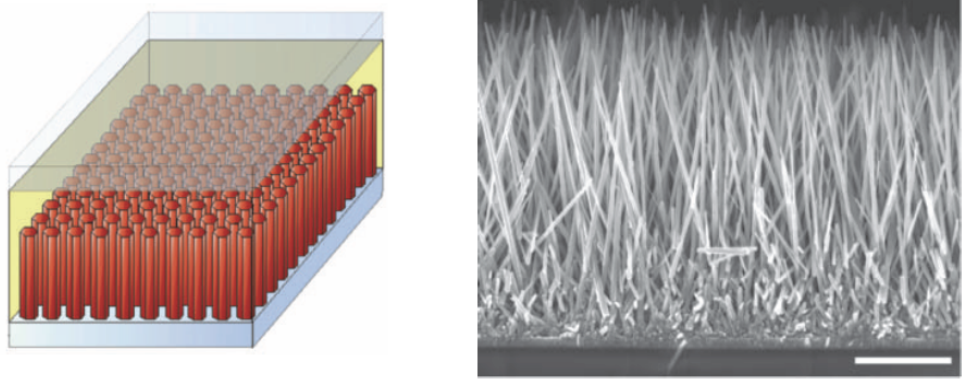

Figure 2-2 The nanowire dye-sensitized cell, based on a ZnO wire array. (a) Schematic diagram of the cell. Light is incident through the bottom electrode. (b) Typical scanning electron microscopy cross-section of a cleaved nanowire array on FTO. The wires are in direct contact with the substrate, with no intervening particle layer. Scale bar, 5 μm.

Feng et al. have reported dye sensitized solar cells fabricated using the nanowire arrays demonstrate very encouraging photoconversion efficiencies, 5.02% for a 2-3 μm long nanowire array as Figure 2-3 illustrated. The IPCE threshold is at 415 nm and the values reach a maximum of approximately 90% at 380 nm, indicating that the nanowire arrays have broad and high light absorption and low charge recombination. The electron mobility of the nanowire arrays is over 2 orders of magnitude larger than those for nanoparticulate TiO_2 films [49, 52]. Hence, the combination of a short hole retrieval length and fast electron transport may account for the excellent charge separation. Unlike nanoparticle-based electrodes that need a positive bias between 0.5 to 1 V (vs reference electrode) to completely separate the light generated electron-hole pairs [50], the photocurrent of the TiO_2 nanowire array-based electrode increases sharply, reaching saturation at approximately -0.25 V, indicative of both low series resistance and facile separation of the photogenerated charges.

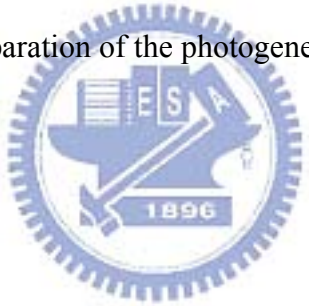

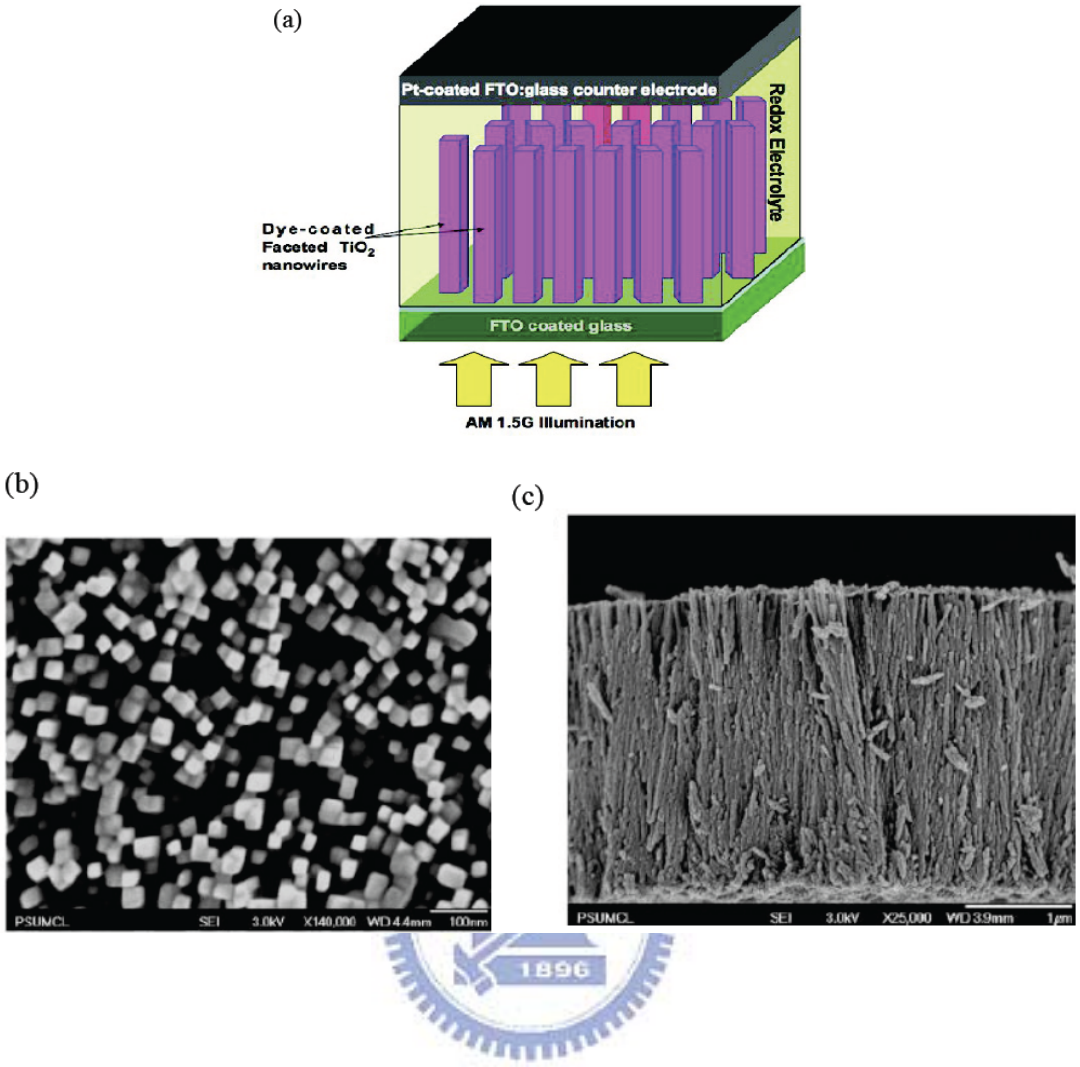

Figure 2-3 (a) Scheme of vertically oriented self-organized TiO_2 nanowire array grown on FTO, (b) top-view FESEM image, and (c) cross-sectional FESEM image.

2.3 Nanotube-Based DSSC

Among 1-D nanomaterials, tubular-structured materials have shown unique chemical and physical properties because of their outer as well as inner surfaces having the "wall" of nanometer thick, their high surface-to-volume ratios, and size dependent properties. The arrangement of the highly ordered titania nanotube array perpendicular to the surface permits facile charge transfer along the length of the nanotubes from the solution to the conductive

substrate, thereby reducing the losses incurred by chargehopping across the nanoparticle grain boundaries [51]. Easier access to the nanotube array surface, as well as better control of the interface makes this morphology desirable for DSSCs [52–54]. The enhancement in the electronic transport also allows for improved light harvesting as thicker films can be used to increase the optical density, thus improving the absorption of low-energy photons in the red and infrared without losing the additionally harvested charge carriers to recombination [57]. Several nanotubular architectures have been investigated for potential enhancement of electron percolation pathways and light conversion as well as improved ion diffusion at the semiconductor - electrolyte interface. We review recent application of these highly ordered nanotube arrays as the working electrode in liquid junction DSSCs.

Highly ordered TiO_2 nanotube arrays of 46-nm pore diameter, 17-nm wall thickness, and 360-nm length were grown perpendicular to a fluorine-doped tin oxide-coated glass substrate by anodic oxidation of a titanium thin film as Figure 2-4 demonstrated [55]. Figure 2-5 is the plot of the response time of the TiO_2 nanotubes DSSC and, for comparison, TiO_2 nanoparticles DSSC replotted from Fabregat-Santiago et al. work [56]. In comparison to reported open circuit photovoltage decay measurements of nanoparticulate TiO_2-based DSSC the transparent nanotubes exhibit superior recombination characteristics, with the longer lifetimes indicating fewer recombination centers in the nanotubular films.

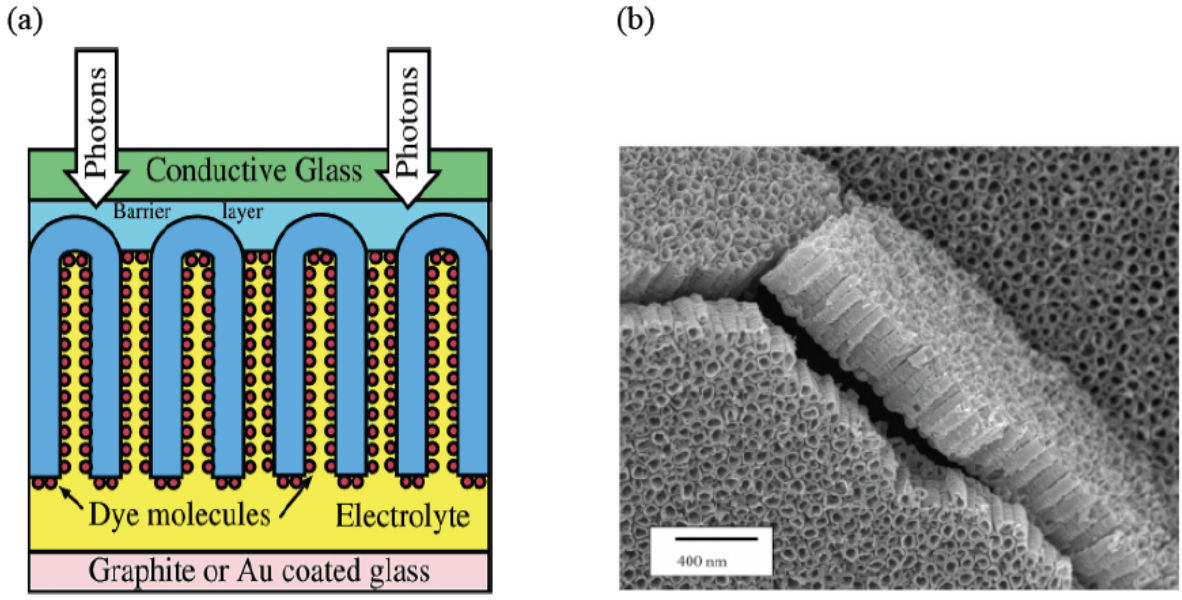

Figure 2-4 Integration of transparent nanotube array architecture into dye solar cell structure. Lateral view FESEM image of titanium nanotubes grown from a 500-nm-thick Ti thin film anodized using a 0.5% HF electrolyte concentration at a potential of 12 V.

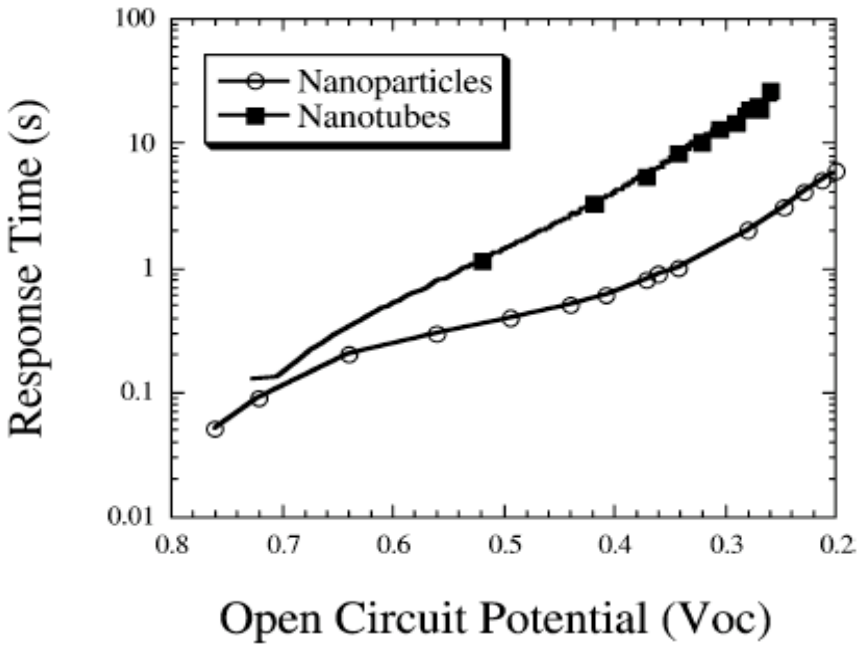

Figure 2-5 Response time determined by open circuit photovoltage decay for a transparent TiO_2 nanotube-based DSSC as well as response times for a TiO_2 nanoparticle-based DSSC.

Kai Zhu et al. [57] have reported on dynamics of electron transport and recombination in dye-sensitized solar cells incorporating oriented TiO_2 nanotube arrays. The transport and recombination times of electrons in nanotubes (NT) and nanoparticles (NP) films were compared in Figure 2-6. Although the transport times for both film morphologies are comparable, the recombination time constants for the NT arrays are an order of magnitude larger than those for the NP films. The slower recombination could indicate that fewer potential surface recombination sites exist in NT arrays than in NP films, given that the charge-collection efficiency for NT electrodes must be significantly greater. The short-circuit photocurrent density (J_{sc}) dependences of the NT and NP films on film thickness were also investigated in Figure 2-7. The photocurrent density is seen to increase linearly with the thickness of both NT and NP films. However, the rate of increase of J_{sc} with L is larger for the NT films than for the NP films, indicating that the charge-collection efficiency of the NT photoelectrodes was markedly enhanced.

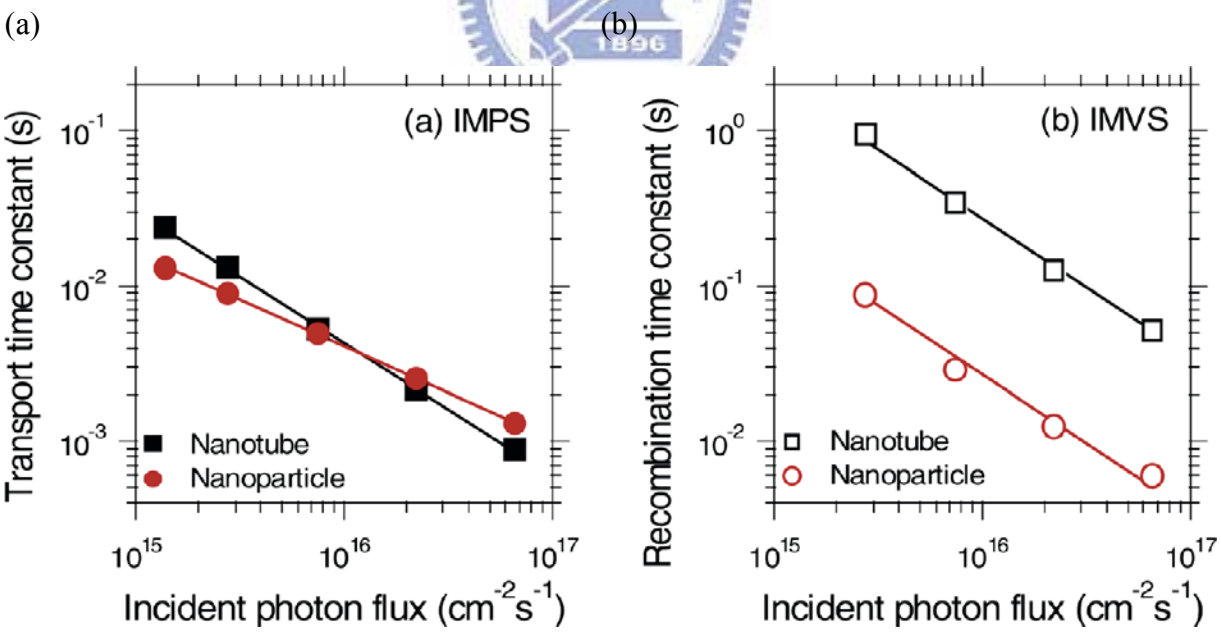

Figure 2-6 Comparison of (a) transport and (b) recombination time constants for NT- and NP-based DSSCs as a function of the incident photon flux for 680 nm laser illumination.

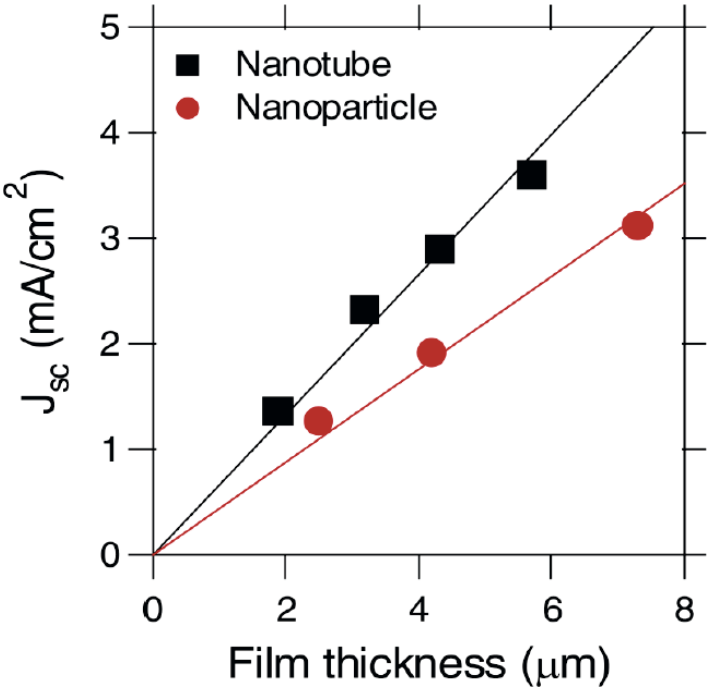

Figure 2-7 Comparison of the short-circuit photocurrent densities of dye-sensitized NT and NP cells as a function of film thickness.

2.4 Anodic Aluminum Oxide (AAO) Applied in DSSC

A strategy used in the fabrication of nanotubes or rods involves template-directed synthetic methods. Typically this involves the fabrication of a nanoporous template, backfilling with the material of interest, and then yields the resulting nanostructure. While many templates have been and continue to be investigated, the use of anodized alumina could provide a low-cost approach that is quite versatile in achieving controllable pore size and shape. Electrochemically anodizing aluminum in an aqueous, acidic solution results in the growth of an alumina film on the surface of the aluminum substrate. Under appropriate conditions, the alumina forms a highly ordered scaffold consisting of a nanostructure array of cylindrical pores oriented perpendicular to the substrate. The pore diameter and aspect ratio of this template can be controlled simply by adjusting the anodization conditions. A variety of

approaches have been studied as a means to backfill the template including electrophoresis, electrochemical deposition, and solution infiltration, and this has resulted in a variety of oxide nanostructures being formed [58-60]. Chu and co-workers have had some success in fabricating TiO_2 nanotubes on a glass substrate by anodizing a sputtered aluminum substrate and using sol-gel infiltration [61].

Recently, Hupp and co-workers [62] employed ZnO nanotubes with anodic aluminum oxide (AAO) as photoanodes for use in DSSCs. The ZnO nanotube arrays were fabricated on a 60-μm-thick membrane with 200 nm pores (Anodisc, Whatman) by the ALD technique as Figure 2-8 indicated. Under AM1.5 illumination the most efficient cell gives a J_{sc} of 3.3 mA/cm^2, V_{oc} of 739 mV, and fill factor (FF) of 0.64, yielding an overall conversion efficiency of 1.6%, Figure 2-9. Compared to similar ZnO-based devices, ZnO nanotube with anodic aluminum oxide (AAO) cells show exceptional photovoltage and fill factors.

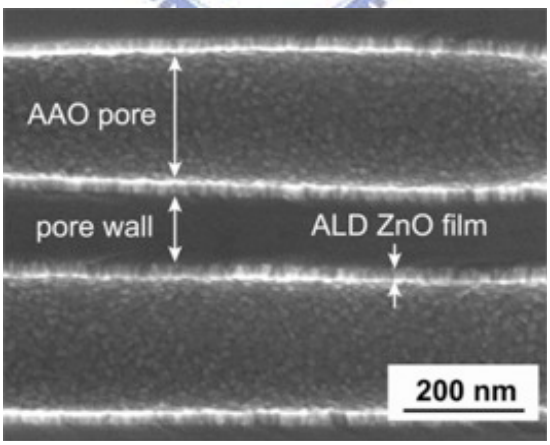

Figure 2-8 Cross-sectional SEM image of commercial AAO membrane pores coated with 20 nm of ZnO by ALD.

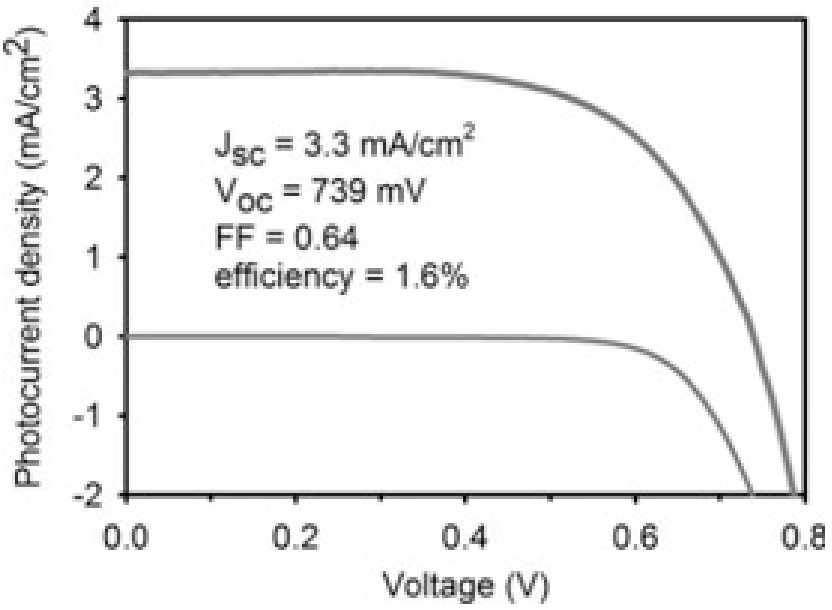

Figure 2-9 I-V curves for the most efficient cell, 7 nm ZnO, under simulated AM1.5 illumination.

In 2008, Martinson and co-workers [63] reported a new photoelectrode architecture consisting of concentric conducting and semiconducting nanotubes for use in dye-sensitized solar cells. Atomic layer deposition was employed to grow indium tin oxide (ITO) within anodic aluminum oxide (AAO) and subsequently coated the high area photoelectrode with amorphous TiO_2 as Figure 2-10 and Figure 2-11 show. The DSSC exhibits a J_{SC} of 2.6 mA/cm^2, V_{OC} of 716 mV, and fill factor (FF) of 0.58, yielding an overall conversion efficiency of 1.1%. Compared with control devices lacking a current collector within the pores, the new photoelectrode geometry exhibits dramatically higher current densities, an effect attributed to the radial collection of electrons. These systems are good candidates for the exploration of alternative redox shuttles and previously unexplored semiconducting materials due to their potential for fast electron collection via adjacent electrode.

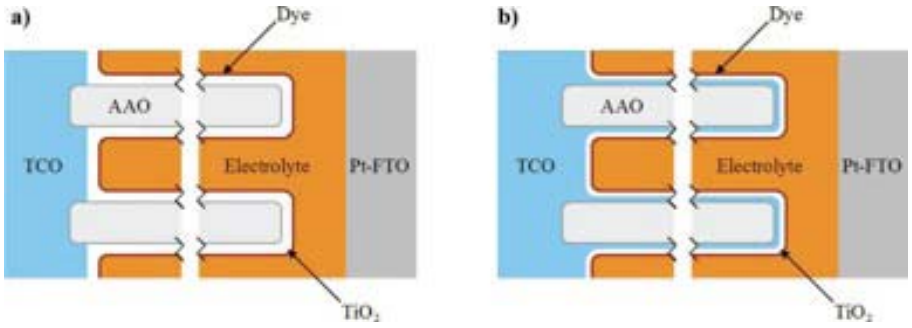

Figure 2-10 Idealized two-dimensional cross section of (a) a nanotube DSSC photoanode and (b) a concentric nanotube DSSC photoanode with ITO lining the pores.

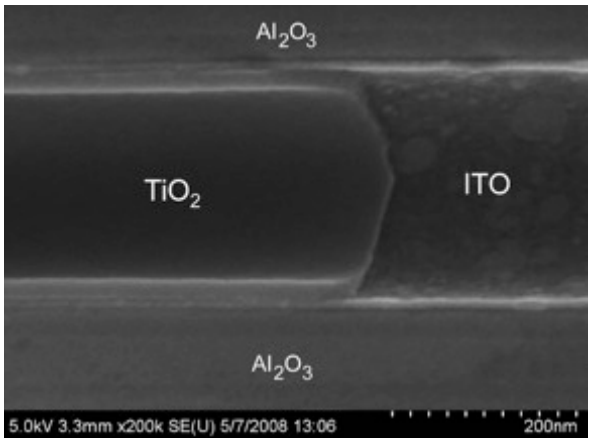

Figure 2-11 Cross-sectional SEM image of a TiO_2 tube cleaved to reveal the i-ITO tube beneath. The concentric tubes, grown by atomic layer deposition, are embedded in a 60 μm long alumina pore. In order to provide clear imaging, the TiO_2 and i-ITO film thicknesses shown here are thicker than those utilized in photovoltaic devices.

2.5 Hollow Sphere-Based DSSC

In order to satisfy the requirements for fast electron transport and high surface area in thin-film photoelectrodes, Yang and his co-workers [64] combined colloidal templates and rf-sputtering to deposit quasi-ordered hollow TiO_2 hemispheres on conducting glass substrates. Enhanced photoconversion efficiency was obtained due to the predominant role of the hollow structure in promoting electron transport [65] as well as a large surface area for enhanced dye loading. The scheme in Figure 2-12 illustrates the procedure used to fabricate the DSSCs.

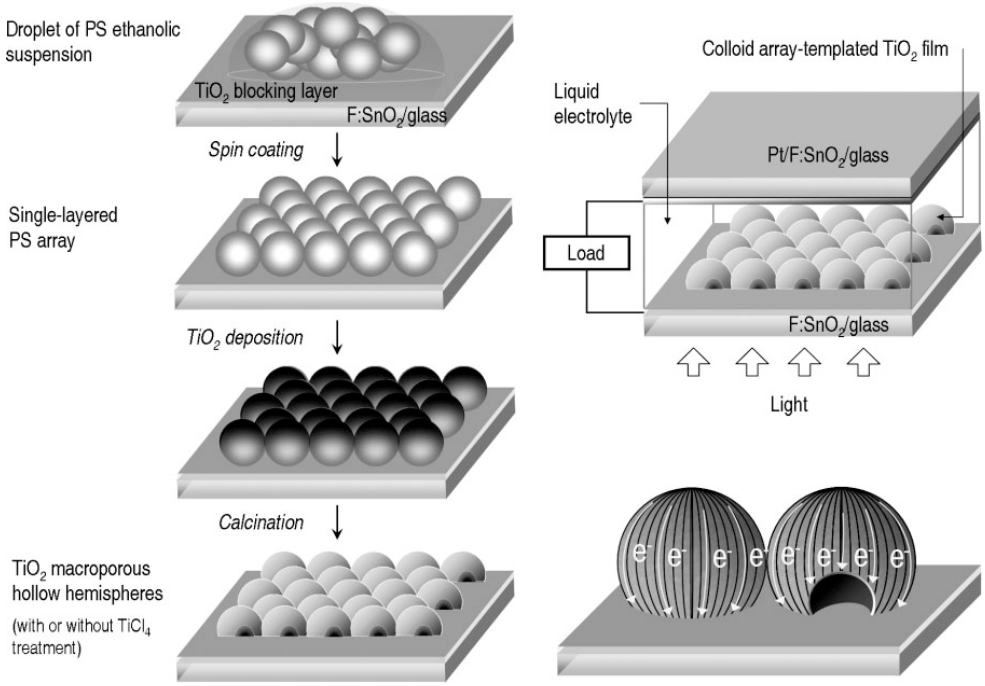

Figure 2-12 Schematic diagrams of the procedure used to fabricate the DSSCs. a) Formation of hollow TiO_2 hemisphere photoelectrode using a colloidal templating route combined with an rf-sputtering method. b) Integration of hollow TiO_2 hemisphere photoelectrode into a dye solar cell structure. c) A model for the electron transport path through a quasi-ordered hollow TiO_2 hemisphere structure.

Figure 2-13 shows FE-SEM images of the TiO_2 electrodes obtained by this colloidal template method. Hollow hemisphere diameter and shell thickness were about 1.65 μm and 120 nm. The films consisted of a monolayer of hollow hemispheres with diameters commensurate with that of the original PS microspheres (1.76 μm). The specific surface area was at least twice as large (inner and outer surfaces), and the surface area four times as large as films deposited on planar untreated substrates. Unlike plain films where only the outer surface contributes to the electrode's activity, here the inner surface within the hemisphere also contributes because it can readily adsorb dye molecules. It is important to note that the $TiCl_4$ treatment made the surface of the TiO_2 hemispheres much rougher as compared to that of untreated TiO_2 hemispheres. An enlarged contact area between hollow TiO_2 electrodes and substrates after a $TiCl_4$ treatment could serve to provide an efficient electron transport to the FTO glass. The conversion efficiency of the cell was found to increase from 1.27% for the 120 nm thick films to 2.44% for 1.36 μm thick films, respectively. Furthermore, the $TiCl_4$-treated TiO_2 DSSCs exhibited a markedly enhanced conversion efficiency of 3.49% while retaining a thin layer of less than 2 μm.

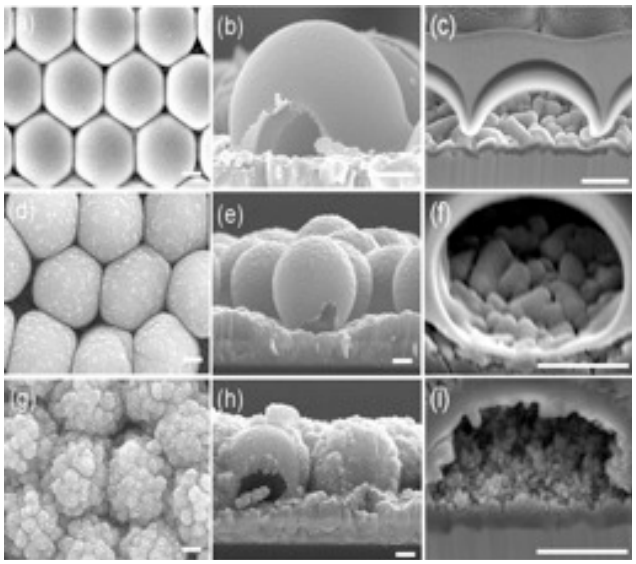

Figure 2-13 Scanning electron micrographs of quasi-ordered hollow TiO_2 hemispheres. (a) Top view of the quasi-ordered hollow hemisphere structure with a hexagonal distribution. (b) Side view of a single TiO_2 hemisphere. (c) Cross sectional view of TiO_2 hemispheres micromilled by focused ion beam. (d) Top, (e) side and (f) cross-sectional view of a monolayer film of 1.36 μm thick TiO_2 hemispheres, respectively. (g) Top, (h) side and (i) cross-sectional view of a monolayer film of 1.36 μm thick TiO_2 hemispheres after a $TiCl_4$ treatment, respectively. All scale bars represent 500 nm.

Koo et al. reported on nano-embossed hollow spherical TiO_2 (NeHS TiO_2) for use in high-efficiency dye-sensitized solar cells as Figure 2-14 shows. This is the first demonstration of a bifunctional material exhibiting efficient generation of photo-excited electrons as well as good light-scattering property. DSSC based on a nanocrystalline (ca. 8 μm)/NeHS (ca. 7 μm) bilayer structure, where a J_{SC} of 17.8 mA/cm^2, V_{OC} of 845 mV, FF of 68.9%, and an overall energy-conversion efficiency of 10.34% are obtained under one sun light intensity at AM 1.5G condition. Figure 2-15 shows the absolute IPCE of 1L-NeHS (the thin nanocrystalline TiO_2-layerbased NeHS TiO_2 overlayer) is higher than that of 1L-CCIC (flat-surface

submicrometer-sized TiO_2 particles) over the entire wavelength region, which is in good agreement with the observed higher J_{SC}. Because of its bifunctional characteristics, nano-embossed hollow spherical TiO_2 can be utilized as an efficient material for high-efficiency dye-sensitized solar cells. The combination of 1-D with 0-D nanostructures is attracting more and more interests in enhancing efficiencies of dye sensitized solar cells.

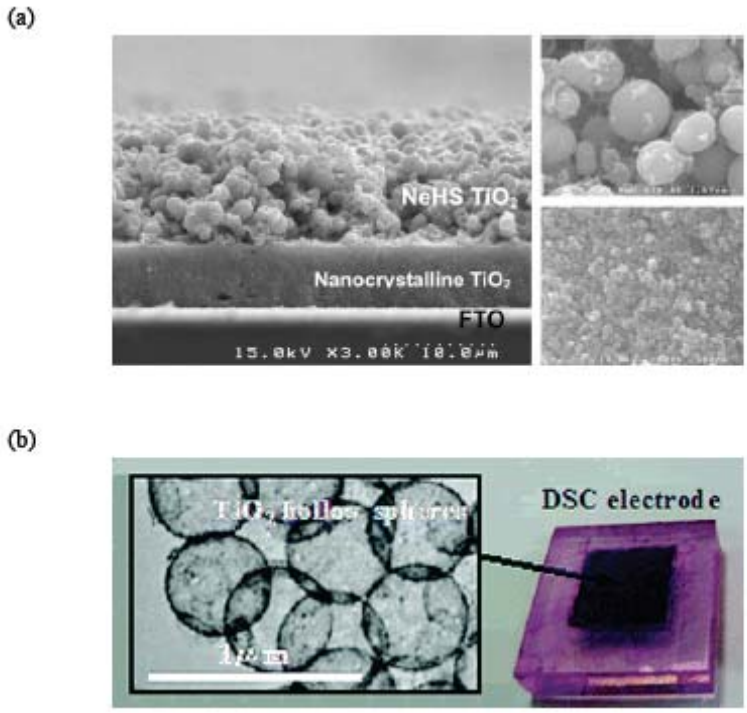

Figure 2-14 (a) Cross-sectional and top-view SEM images of a bilayer structure showing the nanocrystalline TiO_2 underlayer and the NeHS TiO_2 overlayer. (b) TEM image of nano-embossed hollow sphere TiO_2 applied electrode.

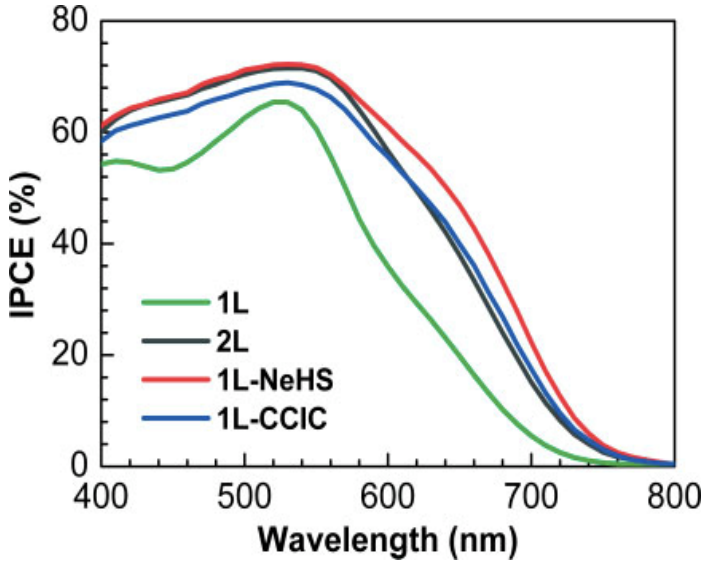

Figure 2-15 Incident-photon-to-current conversion efficiency (IPCE) spectra of DSSCs based on nanocrystalline TiO_2 films of ca. 6 μm thickness (1L) and ca. 12 μm thickness (2L) and the 1L-based bilayer structure having an overlayer of nano-embossed hollow sphere TiO_2 particles (1L-NeHS) and flat-surface submicrometer-sized TiO_2 particles (1L-CCIC).

2.6 Motivation

The development of solar energy devices as an alternative to nonrenewable power sources remains a focus of many groups seeking to provide solutions to rapidly increasing global energy demands. Photovoltaic systems based on nanostructures are currently attracting widespread attention because of their potential for low cost and high-throughput manufacturing. Dye-sensitized solar cells (DSSC) based on a TiO_2 working electrode with an adsorbed ruthenium complex have exhibited power conversion efficiencies over 11% [35] and remain one of the most promising device paradigms. The ability to fabricate the nanoscale architecture of the TiO_2 network is expected to positively impact solar cell performance by providing more direct migration pathways with improved charge transport efficiencies, as well as simplified device architectures. Furthermore, the creation of nanostructured electrodes

is receiving widespread attention and could have significant influence in such diverse areas as photocatalysis, chemical sensing, and biotechnology [66-68].

TiO_2 nanotubes using porous anodic aluminum oxide (AAO) to backfill the template with TiO_2 precursor showed a lot of advantages in DSSC application [69]. TiO_2 nanotubes are formed along the channels and separated by isolation alumina. The divided nanotubes without interconnections improve electron transport leading to higher photoefficiencies; plus, the alumina layer slows the recombination of the photo-generated electrons on the TiO_2 conduction band and holes in the electrolyte or the oxidized dye [63]. In most cases, AAO was fabricated through anodization of foil aluminum. After deposition of TiO_2 nanotubes, the AAO/TiO_2 complex capped onto fluorine-doped tin oxide (FTO) substrate. However, the poor contact between FTO and AAO may cause a serious leakage of electron transport.

To overcome this drawback, one ideal solution is the deposition of stable AAO templates directly on FTO substrates. Al anodization on FTO glass is a key that has promoted AAO-assisted deposition of nanomaterial arrays extending from FTO that are attractive for a range of opto-electronic applications. Unfortunately, sparks and gas evolution were reportedly observed as the anodization proceeded down to the Al/FTO interface due to the oxide barrier layer and the delamination of alumina. We have concentrated on the anodization behavior of the interface between Al and Ti on FTO substrate and found an interesting result. Before anodization, a thin titanium film was coated between Al and FTO substrate. Anodizing reaction proceeds in the sequence of growth of porous anodic alumina when the aluminum layer is consumed up to the underlying Ti, growth of hollow TiO_2 hemispheres under the bottoms of the alumina pores spontaneously occurred. The TiO_2 hemisphere not only prevents the delamination of Al from FTO but also prohibit the formation of thick barrier layers at the bottom of the pore channels. The most important thing is that, we suppose, TiO_2 hemispheres show the improvement of charge transport efficiencies and hence make positive impact on DSSC performance. Figure 2-16 shows the scheme of the novel architecture.

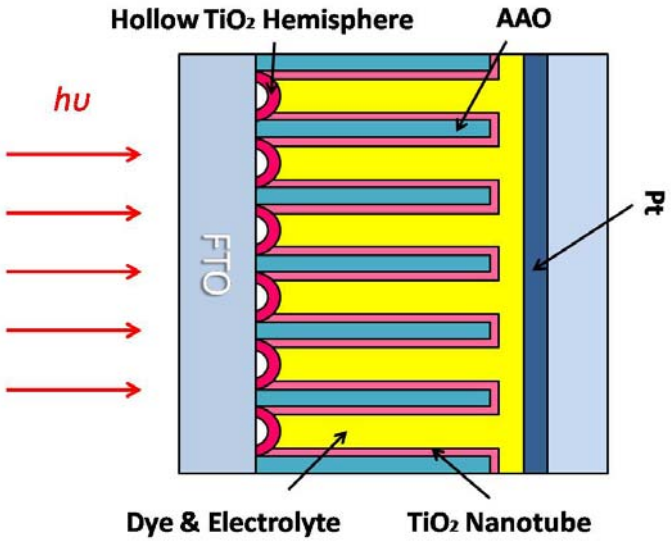

Figure 2-16 Scheme of novel architecture applied in DSSC electrode: self-organized hollow TiO_2 hemispheres under porous alumina with TiO_2 nanotubes inside.

Chapter 3: Experiment

3.1 General Introduction

The fabrication process flow is depicted as Figure 3-1. In this work we investigate effects of electrode film morphology on performance of a DSSC by comparing cells based on different working electrodes structures. We proposed a novel structure consisted of self-organized hollow TiO_2 hemispheres under porous alumina with TiO_2 nanotubes inside (Sample B); other than this structure, four types of TiO_2 nanostructure electrodes were prepared as reference electrodes: self-organized hollow TiO_2 hemispheres under AAO with TiO_2 nanotubes inside and $TiCl_4$ treatment (Sample A), TiO_2 film under AAO with TiO_2 nanotube inside (Sample C), self-organized hollow TiO_2 hemisphere under TiO_2 nanotube (Sample D), and typical TiO_2 nanoparticle (Sample E). The used materials are shown in Table 3-1. All the experiments were preceded in National Chiao Tung University (NCTU).

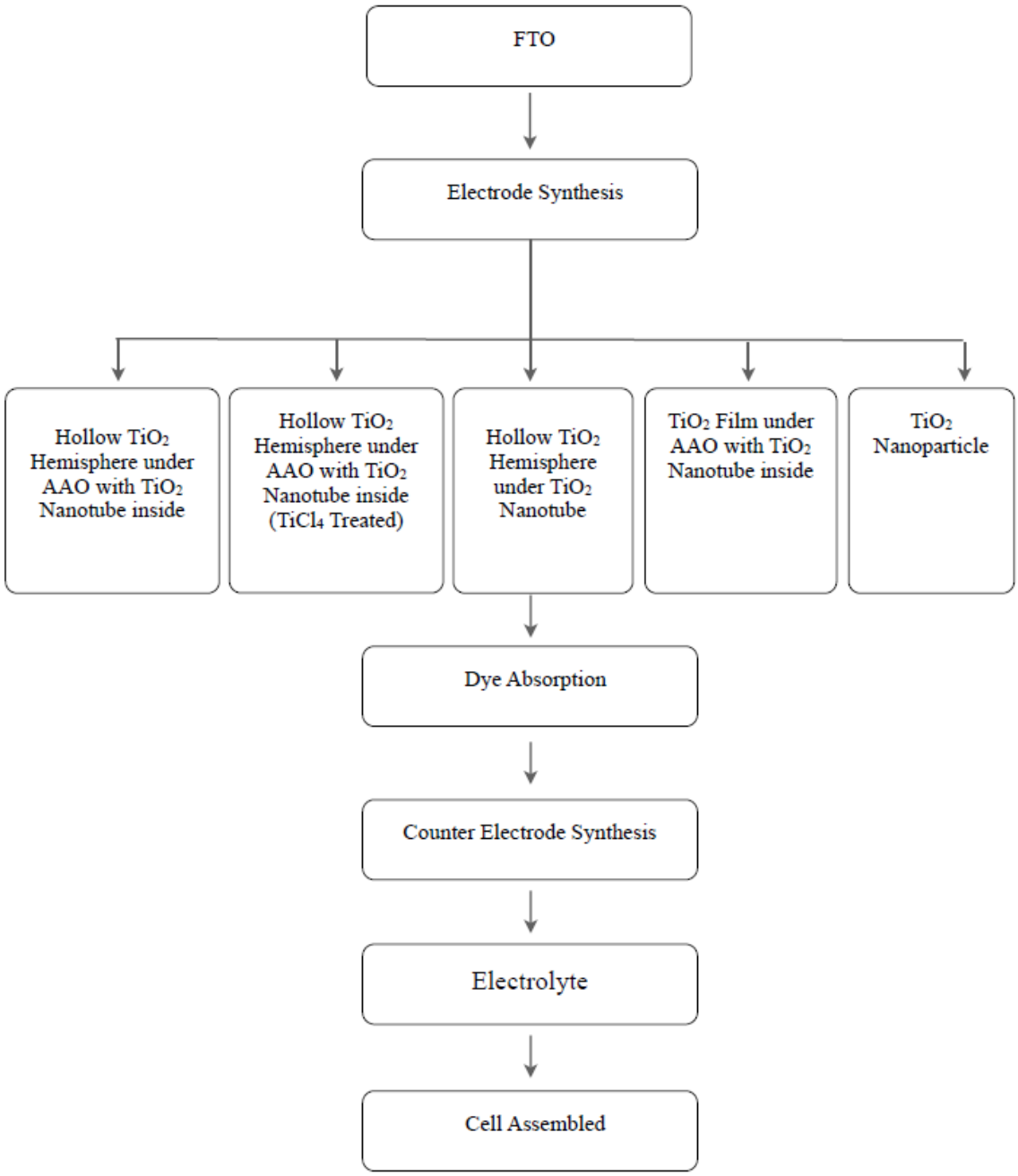

Figure 3-1 The fabrication process flow of various electrodes used in dye-sensitized solar cell.

Substrate		
Type	Thickness	Sheet Resistance
Fluorine-doped tin oxide (FTO)	3 mm	8 Ω / sq
Fluorine-doped tin oxide (FTO)	1.1 mm	10 Ω / sq
TiO2		
Titanium isopropoxide	97%, Aldrich	
P25	Degussa	
Dye		
Ruthenium 35-bisTBA (N719)	Solaronix	
Ionic Electrolyte		
Iodine	98%, Merck	
Lithium iodide	99.93%, Merck	
Tert-butylpyridine	96%, Aldrich	
3-Methoxypropionitrile	99%, Aldrich	
Spacer		
SX1170-25	25 μm	
Others		
Titanium tetrachloride	99.9%, SHOWA	
Absolute ethanol	99.8%, Aldrich	
Phosphoric acid	85.8%, J. T. Baker	
Hydrochloric acid	37%, Aldrich	

Table 3-1 The materials used in this study.

3.2 Syntheses of Nanostructure Electrode

Figure 3-2 shows the schematic diagram of fabrication of nanostructure electrodes. The process started with the deposition of titanium and aluminum films on cleaned FTO glass and AAO were prepared by the two-step anodization of the aluminum films. Hollow TiO_2 hemispheres were spontaneous formed through the anodization. Subsequently, a sol-gel precursor solution of titanium isopropoxide was used to synthesis TiO_2 nanotubes. The TiO_2

nanotubes were treated with $TiCl_4$ to further enlarge their surface areas by creating lots of TiO_2 nanoparticles on the structure.

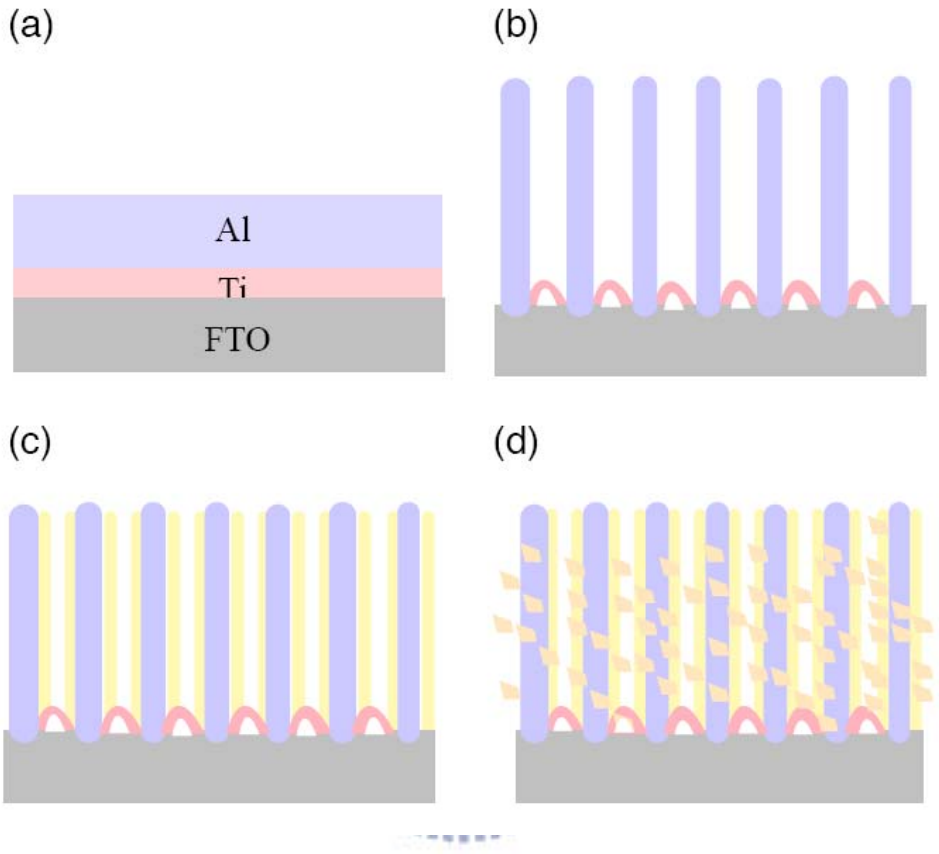

Figure 3-2 Schemes of the procedure of electrode synthesis. (a) Ti and Al films were sputtered on FTO glass. (b) Self-organized hollow TiO_2 hemisphere within AAO was formed after anodization. (c) The growth of titania nanotubes inside AAO with a sol-gel precursor solution of titanium isopropoxide. (d) Roughness of TiO_2 nanotube was increased after $TiCl_4$ treatment.

3.2.1 Anodic Aluminum Oxide Fabrication

The fluorine-doped tin oxide (FTO) substrate (Solaronix) was initially cleaned by sonication in acetone and ethanol, subsequently rinsed with deionized (DI) water, and finally dried in a nitrogen stream. In order to improve the smoothness of the surface for better adhesion of latter deposited materials, the FTO glass was annealed in 450℃ for 12 hr.

The titanium (~35 nm) and aluminum (~1 μm) films were sequentially deposited onto cleaned FTO glass by ultrahigh vacuum dc sputtering system. Subsequently, the sample was annealed under Ar/H_2 ambient at 400°C for 3 hr to reduce the defects, and then electropolished in a 1:3 volume mixture of $HClO_4$ and C_2H_5OH. The mean roughness of the polished surface for enhancing pore organization was measured by atomic force microscopy to be 10 nm over a 4 μm^2 area. Afterward, the Cu support was positioned at the back of the sample while four Cu tapes were used to connect the Cu support and the top Al film. The two-step anodization was used to prepare ordered pore channel arrays of porous anodic alumina. The anodizing process was carried out in an electrolyte of 2 M H_3PO_4 solution at a constant voltage of 110 V. A graphite flake was used as the counter-electrode (cathode). All anodizing process were performed at 5℃ and stirred adequately. Once the anodization was nearly completed, the current dropped distinctly and the color changed on the sample. The anodization was preceded 5 minutes past the color change to form the hollow TiO_2 hemispheres.

Figure 3-3 shows the schematic diagram of experimental setup for the aluminum electropolishing and anodization. A specially designed one-electrode cylindrical cell double layer glass cup was used which can let cooling water flow through. The anode was the aluminum film specimen and a graphite flake was used as the cathode.

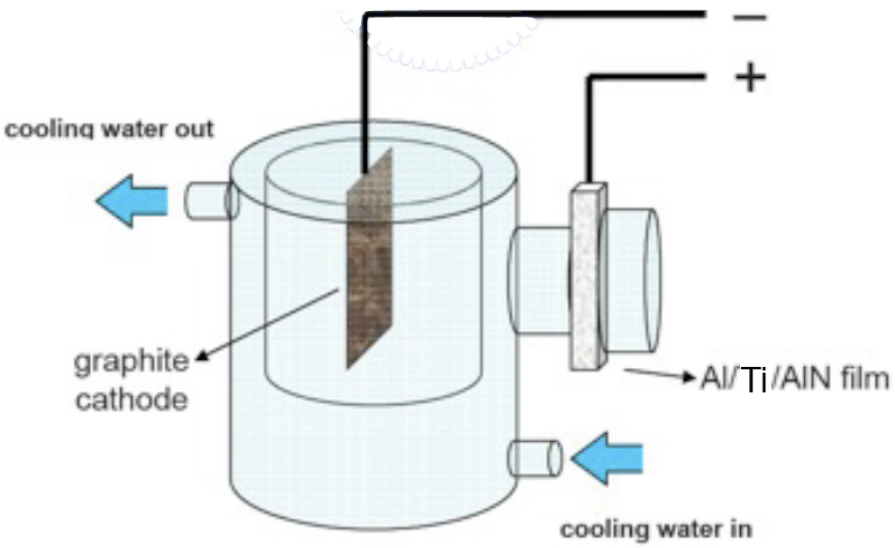

Figure 3-3 The schematic diagram of experimental setup for the aluminum electropolishing and anodization.

3.2.2 TiO_2 Sol-Gel Process

The growth of titania nanotubes with a sol-gel precursor solution of titanium ispropoxide,$Ti(OCH(CH_3)_2)_4$, were previously reported [70]. The anodic alumina on FTO [71] substrates described before were used as templates for the growth of titania nanotubes. 5 mL of titanium isopropoxide ($Ti(OC_3H_7)_4$) (Aldrich) was added to 25 mL of ethanol and then stirred in an ice bath. 0.5 mL of water and 0.5 mL of 0.1 mol/L HCl were added to a second 25 mL portion of ethanol. The $Ti(OC_3H_7)_4/C_2H_5OH$ mixture was removed from the ice bath and then the $C_2H_5OH/HCl/H_2O$ mixture was slowly added at room temperature. The resulting mixture turned milky after ca. 60 s (sol formation). The anodic alumina templates were immediately immersed into this solution for 40 s to form nanotubes and for 1 min to form nanorods. After immersion, the samples were dried by N_2 gas and baked by hot plate at 110℃.

A typical sol solution of $Ti(OC_3H_7)_4$ includes both ethanol and water, plus a variety of other additives. The water acts to hydrolyze the $Ti(OC_3H_7)_4$ which then leads to the formation of TiO_2 particulates in solution (the sol) through a series of condensation reactions which, when brought to completion, results in the formation of the gel. Effects of varying these solution parameters on the structure of both the sol and the gel have been thoroughly investigated [71].

There are tow main steps in the mechanism of $Ti(OC_3H_7)_4$ sol-gel process; the first one is hydrolysis and the other is polycondensation. The reaction is described as below:

Hydrolysis reaction：

-M-OR ＋ H-OH → -M-OH ＋ ROH

Polycondensation reaction：

oxolation：-M-OH＋-M-OX → -M-O-M＋XOH (X=H or R)

olation：-M-OH＋-M ← OX → -M-OH-M＋XOH (X=H or R)

Net reaction:

$nM(OR)_4 + 2n\ H_2O \leftarrow\rightarrow nMO_2 + 4nROH$

Where R and M(OR)n represent alkyl group and titanium isopropoxide.

3.2.3 $TiCl_4$ Treatment

The TiO_2 nanotubes were treated with $TiCl_4$ to further enlarge their surface areas by creating lots of TiO_2 nanoparticles on the structures, thus leading to a higher adsorption of the dye and an improved photogenerated current in the DSSC. Subsequently, the TiO_2 nanotubes were impregnated with a $TiCl_4$ ethanol solution (1:20 v/v) at 70℃ for 3 min followed by baked on a hot plate at 100℃. Repeated three times. Then, it was calcined at 450℃ in air for 6 hr and cooling to room temperature. The heating rate for the calcination steps was 2℃ min. The preparation of the $TiCl_4$ ethanol solution was referred to the previously proposed method [72].

3.2.4 Counter Electrodes

The FTO glass sputter-coated with 30-nm-thick Pt was used as the counter electrode. The platinum films for the counter electrode were deposited on a cleaned FTO glass by our sputtering system (JOEL JFC-1600). Before film deposition, the base pressure of the sputtering chamber was evacuated to approximately 10^{-1} Pa. The Pt films were prepared at argon gas.

3.3 Dye Sensitized and Cell Assembled

Nanotubes were sensitized in absolute ethanol solution containing 6.7 x 10^{-4} M N719 dye for above 12 hr. The dyed electrodes were rinsed with absolute ethanol and dried under an N_2 stream.

The dye-covered TiO_2 electrode and Pt-counter electrode were assembled into a sandwich type cell. The electrode spacing between them was ensured by the use of a 25 μm thick SX-1170 spacer (Solaronix Inc., Switzerland). The electrolyte of 0.5 M LiI, 0.05 M I_2, and 0.5 M tert-butylpyridine in 3-methoxypropionitrile was introduced into the cell via a hole (1-mm diameter) drilled in the counter electrode. A second spacer was sealed over the hole with a soldering iron. Figure 3-4 illustrates the DSSC geometry in the cross section.

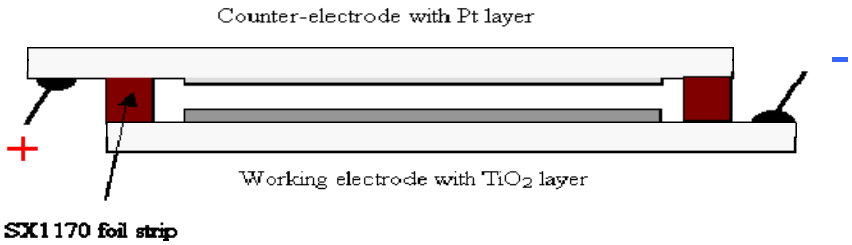

Figure 3-4 Scheme of DSSC in the cross section.

3.4 Materials Characterization

(A) Scanning Electron Microscopy (SEM)

SEM is a very useful tool for observing surface morphology of specimen. SEM has secondary electrons or backscattered electrons detectors passing the signal to computer and forming image. In this study, the morphology and microstructure of the porous alumina films and nanodots were all characterized by a field-emission SEM (FE-SEM) (JEOL-6700) operating at 15 kV accelerating voltage.

(B) Atomic Force Microscope (AFM)

AFM measures inter-atomic interactions between a scanning probe tip and the specimen surface. It can generate topographic images for the specimen surface in atomic scale. In addition, due to its superior vertical and horizontal resolution, AFM are very good for roughness measurement. AFM analyses were performed by a Veeco MultiMode Scanning Probe Microscope system with the contact mode using the silicon nitride (Si_3N_4) tips.

(C) X-Ray Diffraction (XRD)

X-ray diffraction (PANalytical X'Pert Pro) was used to examine the phase composition. X-ray diffraction finds the geometry or shape of a molecule using X-rays. The techniques are based on the elastic scattering of X-rays from structures that have long range order. The most comprehensive description of scattering from crystals is given by the dynamical theory of diffraction.

(D) Cell Performance Measurement (Photocurrent–Voltage Characteristics)

Solar cell performances in this study were examined by two Keithley 2400 source-meter instruments, Keithley 2000 multimeter, Keithley 4200 with a probe station system for device characterization. A solar simulator, including 150 W Xenon lamp, arc lamp power supply and

digital exposure controller, can serve as the standard light source for the photovoltaic devices. UV-vis Cornerstone monochromator with a 300 W Hg light source and silicon and thermopile detectors can be used to investigate the photo-response and photo-action spectra of solar cells.

Chapter 4: Results and Discussion

4.1 Anodization Behavior of Aluminum on FTO Glass

Adhesion improvement between aluminum and FTO substrates is also a function of Ti film, which is in turn dependent upon deposition parameters. When a 30 nm Ti layer was employed, the anodization current was noticeably stabilized, allowing anodization to proceed smoothly down to the substrate. Figure 4-1 shows chronoamperic curves recorded during the anodization of Al on bare FTO glass and on FTO glass coated with Ti layers. The anodization of Al on bare FTO glass was stable within the first 60 s. However, as the anodizing front approached the Al/FTO glass interface (beyond 60 s), there was a sudden surge in current, accompanied by sparks, vigorous gas evolution, and template delamination resulting from the anodic. We attribute this phenomenon to three main reasons: (1) inadequate adhesion between Al films deposited by thermal evaporation on FTO glass; (2) compressive forces in the template due to volume expansion as Al is converted to Al_2O_3, which further weaken the template-to-substrate adhesion; and (3) inevitable pinhole defects that are either present intrinsically or are formed during anodization, through which the electrolyte diffused to the FTO glass surface, causing localized anodic dissolution of FTO glass. The breakdown is so vigorous that sparking occurs and gas bubbles produced break through the template, exposing small areas of bare FTO glass. The dissolution reaction escalates as more areas of FTO glass are exposed, causing eventual delamination of AAO from FTO glass.

Figure 4-2 (a) shows the FTO glass after anodization. The glass substrate with partial transformation of porous alumina without Ti film was displayed. A transparent porous alumina was stripped while the opaque area in the middle was the unreacted Al. Figure 4-2 (b) presents the porous alumina with Ti film after anodization. The complete formation of porous

alumina resulted to entire transparent of FTO glass while the typical anodization without Ti layer was not.

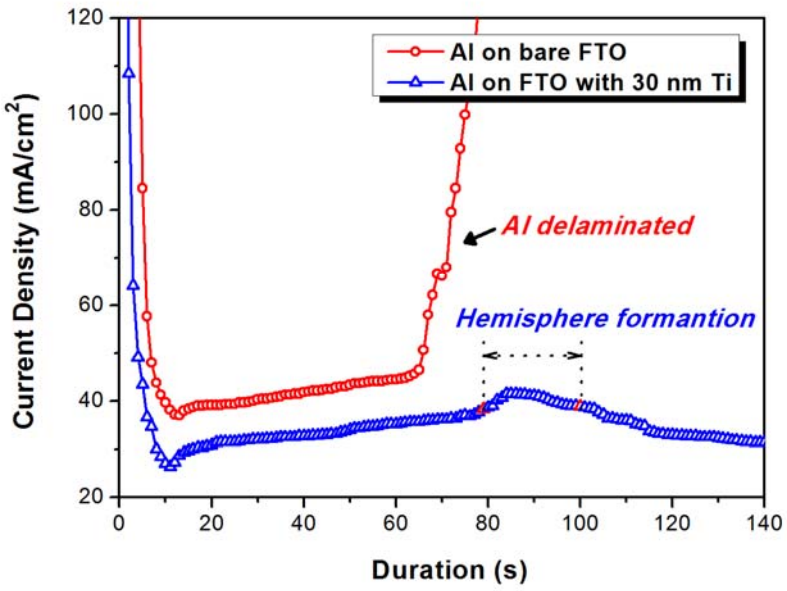

Figure 4-1 Anodization behavior of aluminum (500 nm) coated on various substrates as indicated.

(a) (b)

Figure 4-2 Photographs show the FTO glass after anodization. (a) The glass substrate with partial transformation of porous alumina without Ti film was displayed. A transparent porous alumina was stripped while the opaque area in the middle was the unreacted Al. (b) The glass substrate after complete formation of porous alumina with Ti film was presented. The design advances the uniform current distribution from Ti to Al while the typical anodization without Ti layer localizes the current flow.

4.2 Electrode Morphology Analysis

In this section, we examined the morphological effects of substrate and nanostructure electrode including anodic aluminum oxide and self-organized hollow TiO_2 hemispheres. We illustrated how this topology could improve the understanding and performance of DSSC.

4.2.1 FTO Glass Surface Analysis

Prior to use, FTO glasses were annealed in order to reduce roughness of the surface and hence improve adhesion between titanium and the FTO glass. Figure 4-3 shows AFM image of a blank FTO glass without annealing. The average height of original FTO glass is about

151 nm; after annealing at several conditions: 450℃ for 3 h, 450℃ for 6 hr, 450℃ for 16 hr, and 500℃ for 16 hr, rms height of FTO glass is reduced to 26 nm under the condition of 500℃ for 16 hr (Figure 4-4).

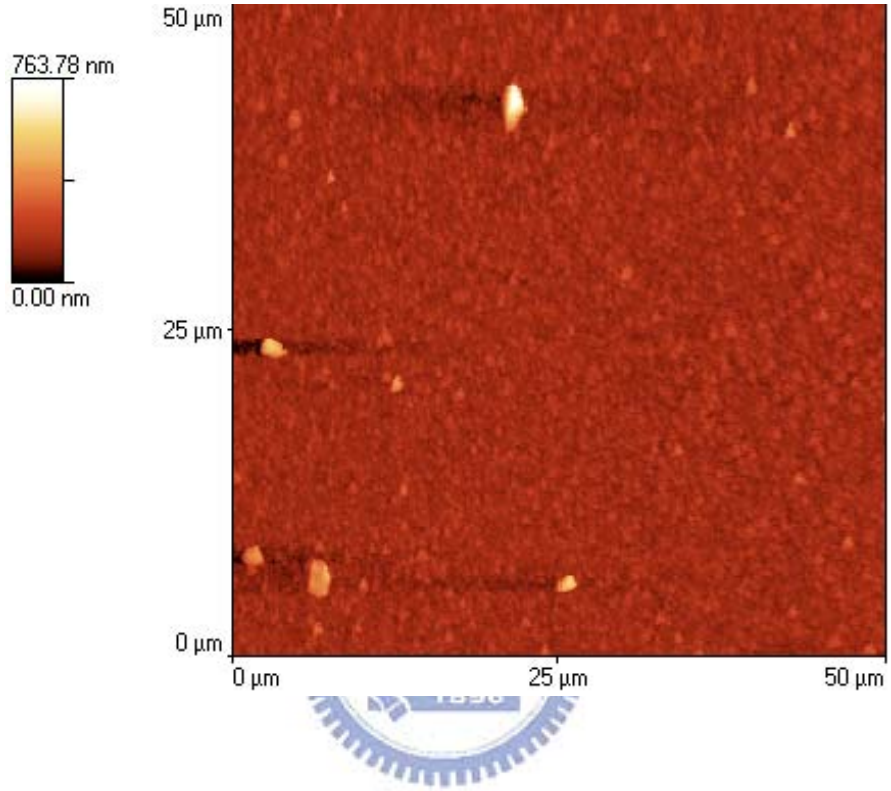

Figure 4-3 AFM image of a blank FTO glass without annealing.

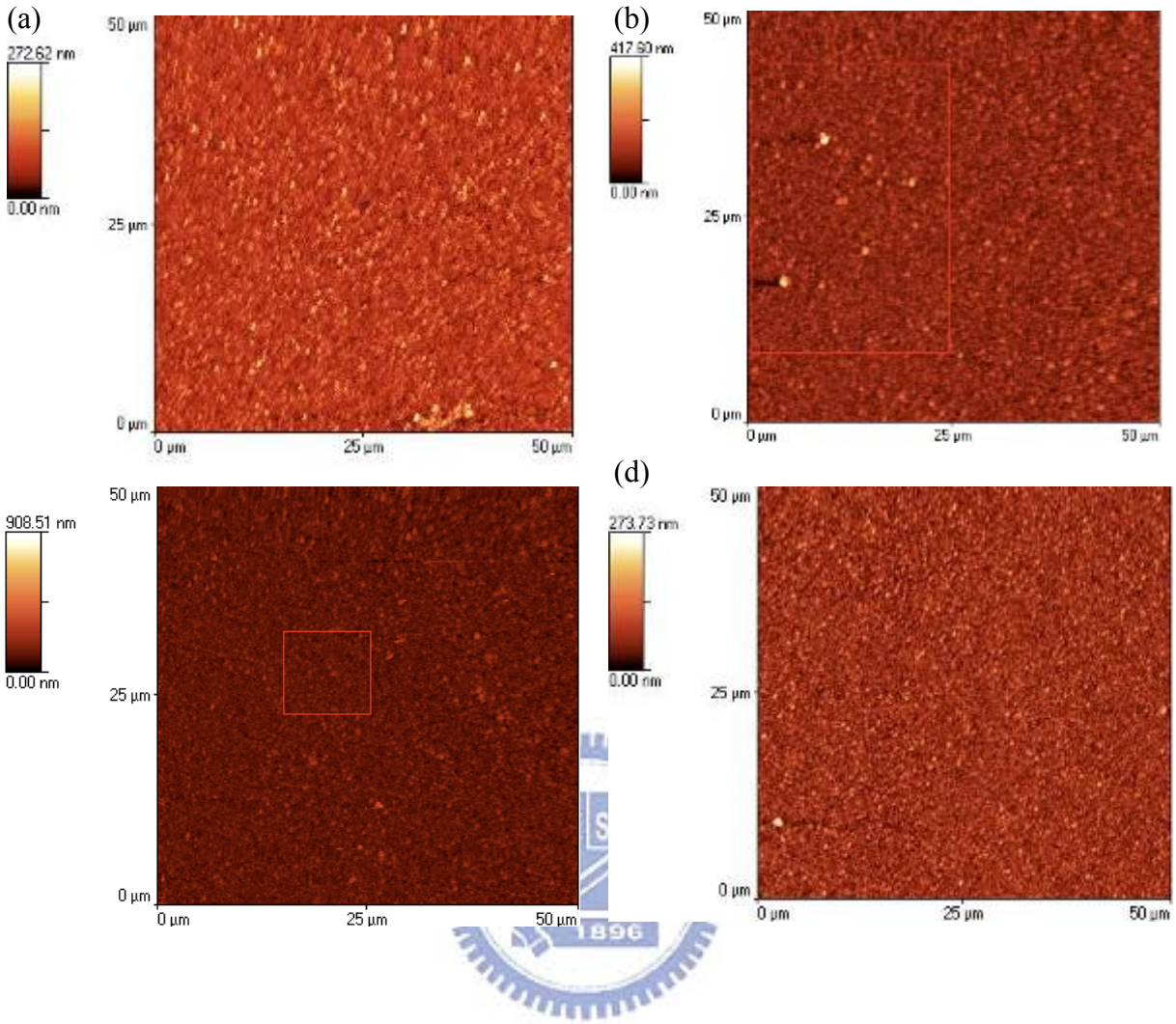

Figure 4-4 AFM image of a blank FTO glass annealed at (a) 450℃ for 3 hr, (b) 450℃ for 6 hr, (c) 450℃ for 16 hr, and (d) 500℃ for 16 hr.

4.2.2 Self-Organized Hollow TiO_2 Hemispheres under Porous Alumina

Figure 4-5 shows the cross-sectional SEM image of anodic aluminum oxide (AAO) with self-organized hollow TiO_2 hemispheres underneath. The AAO grew perpendicularly on substrate with an average inner diameter and length of 200 nm and 700 nm, and accompanied with self-organized hollow TiO_2 hemispheres at a height of 130 nm. Heights of hemispheres were ranged from 50 to 150 nm as the deposited titania and anodization time were increased. The ability to control the nanoscale architecture of the TiO_2 network is expected to positively

impact solar cell performance by providing more direct migration pathways with improved charge transport efficiencies, as well as simplified device architectures. A template-directed synthesis strategy is an ideal tool to fabricate oxide nanotubes in that their physical dimensions can be precisely controlled and monodisperse samples can be harvested in large quantity. As Figure 4-5 illustrated, the AAO template consisted of well-aligned, uniform, cylindrical pores and showed good adhesion to FTO glass, making them highly suitable for subsequent TiO_2 sol-gel synthesis.

The top-view SEM image of self-organized hollow TiO_2 hemispheres formed by anodization after removing the alumina is shown from Figure 4-4. Transparent hollow TiO_2 hemispheres organized on FTO glass act as electrode can enlarge contact area with FTO substrate and hence provide an efficient electron transport to FTO glass [67]. We note that in solar cell application, the nanotube grown directly on FTO coated glass sometimes demonstrated electrical shorting with the redox electrolyte coming into direct contact with FTO layer; in contrary, a hollow TiO_2 hemisphere layer can serve as insulating layer to avoid direct contact between electrolyte and FTO coated glass.

After grinding by emery paper, hollow portion of TiO2 hemisphere was already showed in Figure 4-6 under the bottom of the AAO pores. Films constructed of oriented one-dimensional nanostructures aligned perpendicular to the collecting transparent conductive oxide substrate could potentially improve the charge-collection efficiency by promoting faster transport and slower recombination.

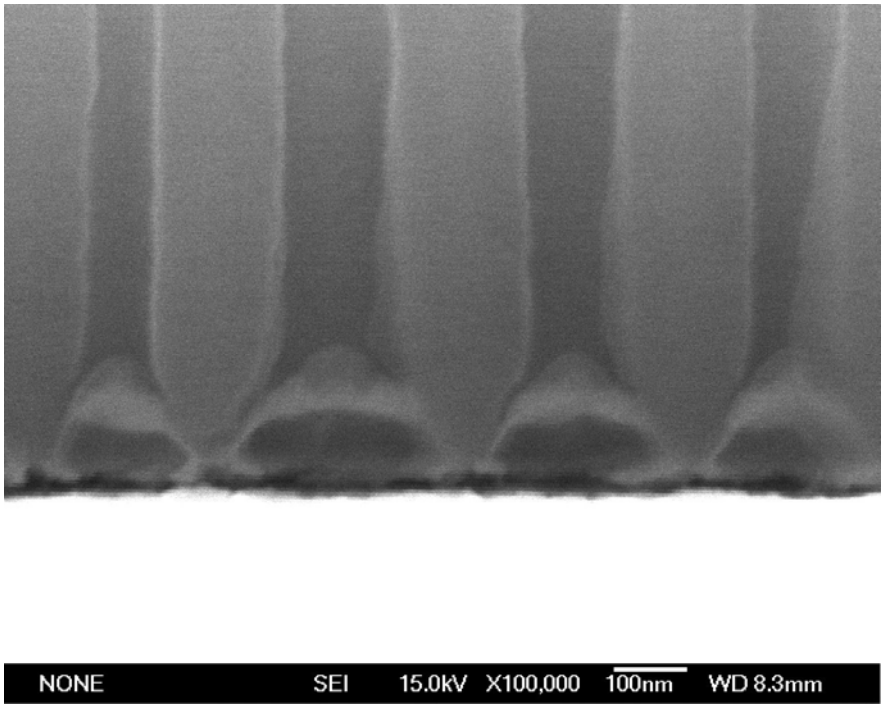

Figure 4-5 Cross-sectional view of SEM image of self-organized hollow TiO_2 hemispheres.

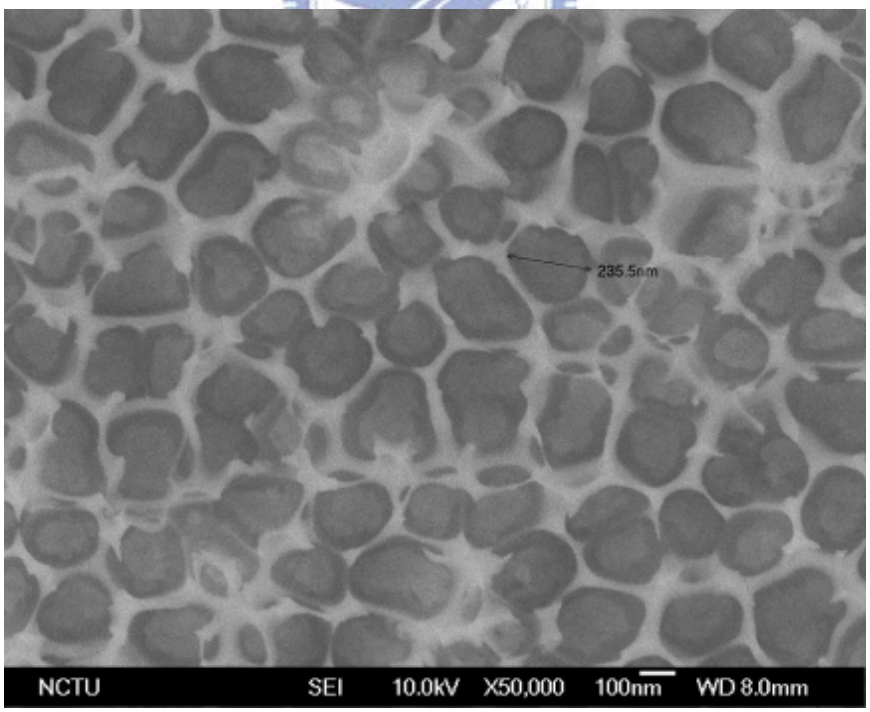

Figure 4-6 Top-view of SEM image of self-organized hollow TiO_2 hemispheres grew directly on FTO glass.

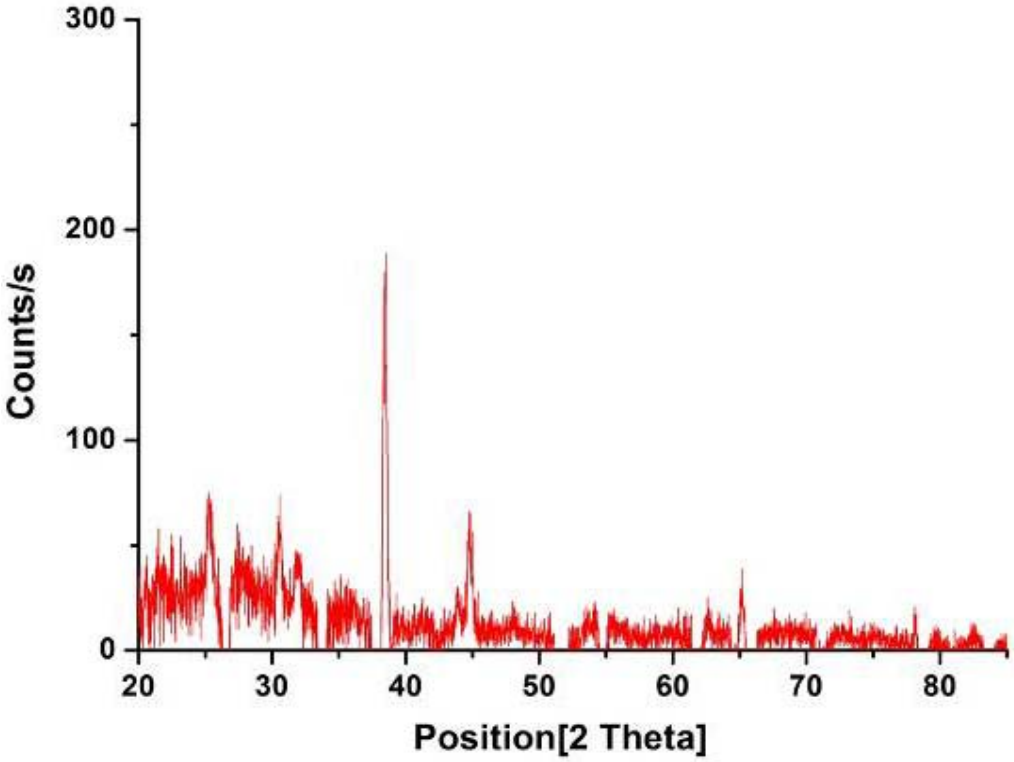

Figure 4-7 X-Ray diffraction pattern of self-organized hollow TiO_2 hemispheres.

From Figure 4-7 can be seen that the self-organized hollow TiO_2 hemisphere was confirmed to be anatase TiO_2 wich is of considerable interest for photocatalysis in dye-sensitized solar cell [73]. Since anatase is better than rutile and brookite for solar energy conversion, the anatase phase is favorable in the preparation of TiO_2 photoanode.

4.2.3 TiO_2 Nanotube

TiO_2 nanotube formed by titanium isopropoxide sol-gel process is shown in Figure 4-9. The height is about 700 nm and the tube diameter is 200 nm as AAO is. With varied periods AAO immersed in titanium isopropoxide solution, TiO_2 nanotubes (Figure 4-8 and Figure 4-9) and nanorods (Figure 4-10) were obtained. Figure 4-9 reveals that TiO_2 nanotubes were

hollow and grew along self-organized hollow TiO_2 hemispheres under AAO. With the aid of AAO, TiO_2 nanotubes presented without any bundles or microcracks which occurred elsewhere [74]. This architecture allows electrons to transfer more directly through well-aligned pathway of TiO_2 nanotube and hence would improve the performance of DSSC.

The arrangement of the highly ordered TiO_2 nanotube array perpendicular to the surface permits facile charge transfer along the length of the nanotube from the solution to the conductive substrate, thereby reducing the losses incurred by charge hopping across the nanoparticle grain boundaries [51]. Easier access to the nanotube array surface, as well as better control of the interface makes this morphology desirable for DSSCs [51–54]. The enhancement in the electronic transport also allows for improved light harvesting as thicker films can be used to increase the optical density, thus improving the absorption of low-energy photons in the red and infrared without losing the additionally harvested charge carriers to recombination.

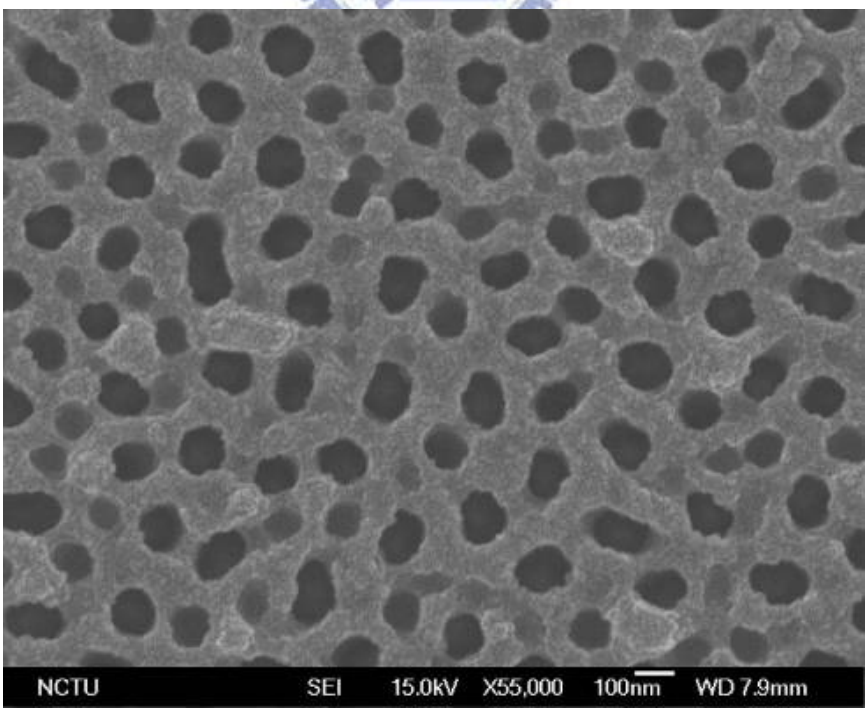

Figure 4-8 Top-view of SEM image of TiO_2 nanotubes with AAO template.

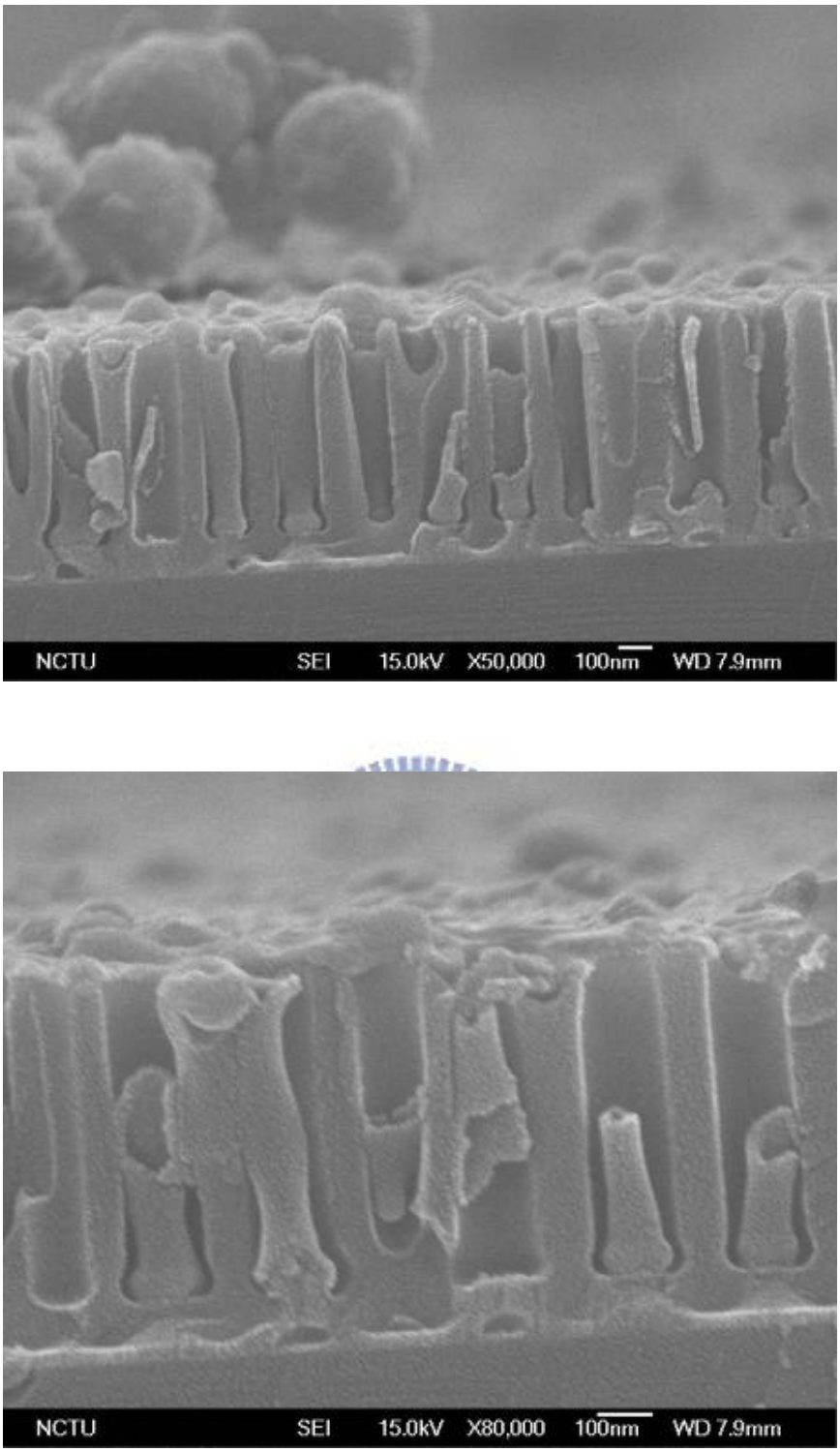

Figure 4-9 Cross-sectional SEM images of TiO_2 nanotubes with AAO template

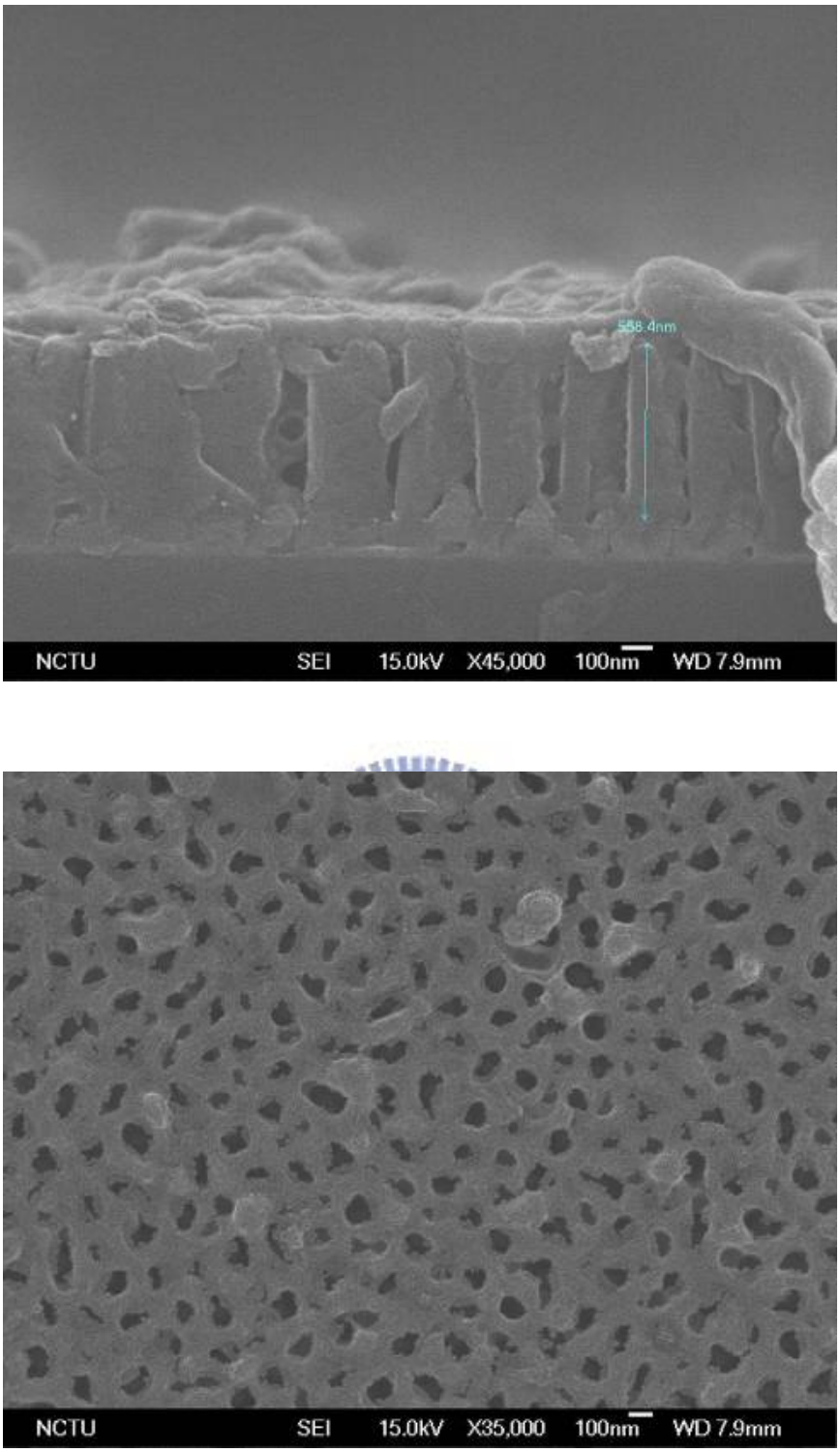

Figure 4-10 SEM image of TiO_2 nanorods with AAO template.

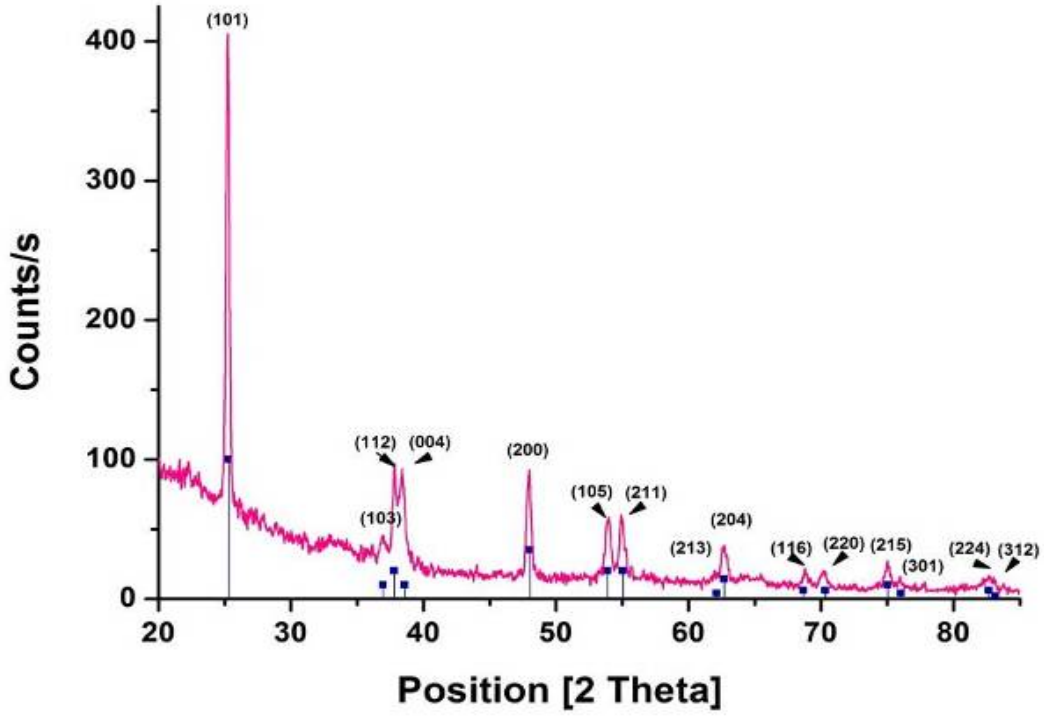

Figure 4-11 X-Ray diffraction (XRD) pattern of TiO_2 nanotubes formed by sol-gel synthesis.

The anatase phase TiO_2 is well known as a good candidate for photoelectrodes. As-deposited amorphous TiO_2 nanotubes were converted to the anatase phase by annealing at 450°C in air for 5 hr. It is noteworthy that there is no evidence that the rutile phase could be observed in the XRD analysis. From Figure 4-11, the enhanced (101) peak at $2\theta = 25.3°$ indicates the nanotube was well crystallized. Applying the Scherrer equation revealed an average crystallite size of 28 nm.

4.2.4 Influence of $TiCl_4$ Treatment

With sufficient understanding of TiO_2 nanotubes properties, it is meaningful to discover the effect from the advanced treatment and structurel modification. A known method to improve the performance of the solar cells is a post-treatment of TiO_2 structures in which an extra layer of TiO_2 is grown onto TiO_2 nanotubes constituting the electrode. The treatment of titanium tetrachloride solution on TiO_2 nanostructures has been confirmed to be able to improve the conversion efficiency of DSSC. Various explanations of the working principle of this coating have been reported. These hypotheses concern increased surface area, improved electron transport [21], light scattering [75], TiO_2 purity, and dye anchoring.

Figure 4-12 and Figure 4-13 show the $TiCl_4$ treatment. TiO_2 nanotubes treated by $TiCl_4$ for 3 min and for 5 min and then baked at 110℃ and subsequently were repeated immersion for 5 times. It is important to note that the $TiCl_4$ treatment made the surface of the TiO_2 nanotubes much rougher as compared to that of untreated ones. The treatment further enlarge their surface areas by created lots of TiO_2 nanoparticles on nanotubes, thus leading to a higher adsorption of the dye and an improved photogenerated current in DSSC. Obviously, the one immersed for 5 min is much rougher than the other for 3 min. However, with more repeated immersion time over than 10 minutes, over etching nanotubes were observed; as Figure 4-14 illustrated, nanotubes walls were flimsy. Optimal parameters were obtained here.

From figure 4-15 we noted that after $TiCl_4$ treatment, pores of TiO_2 nanotubes were still remained which indicated that the dye and the electrolyte were easily impregnated into TiO_2 nanotubes without covering over pores.

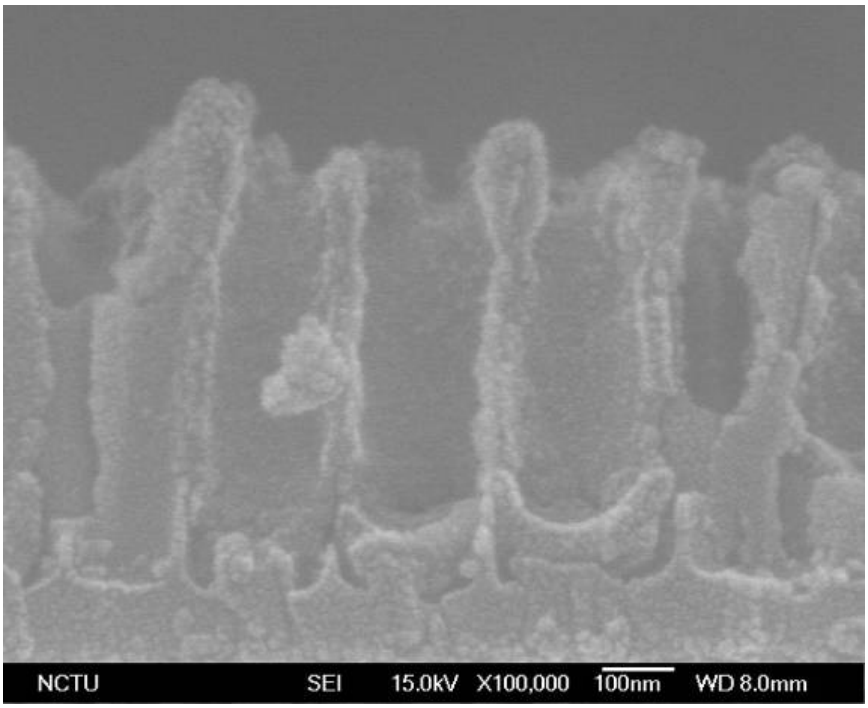

Figure 4-12 Cross-sectional SEM image of TiO_2 nanotubes treated by $TiCl_4$ for 5 min and repeated 3 times.

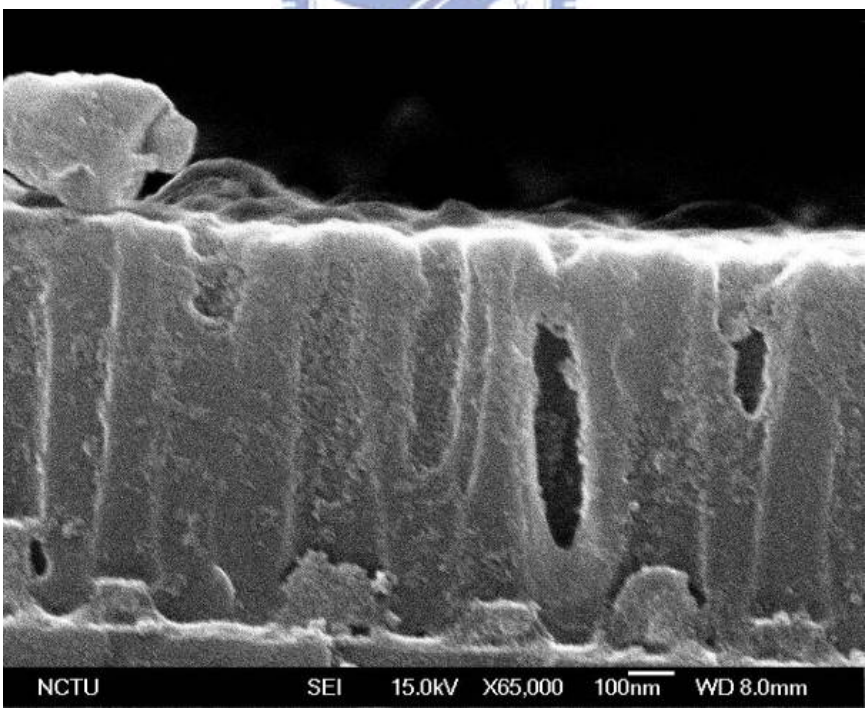

Figure 4-13 Cross-sectional SEM image of TiO_2 nanotubes treated by $TiCl_4$ for 5 min and repeated 5 times.

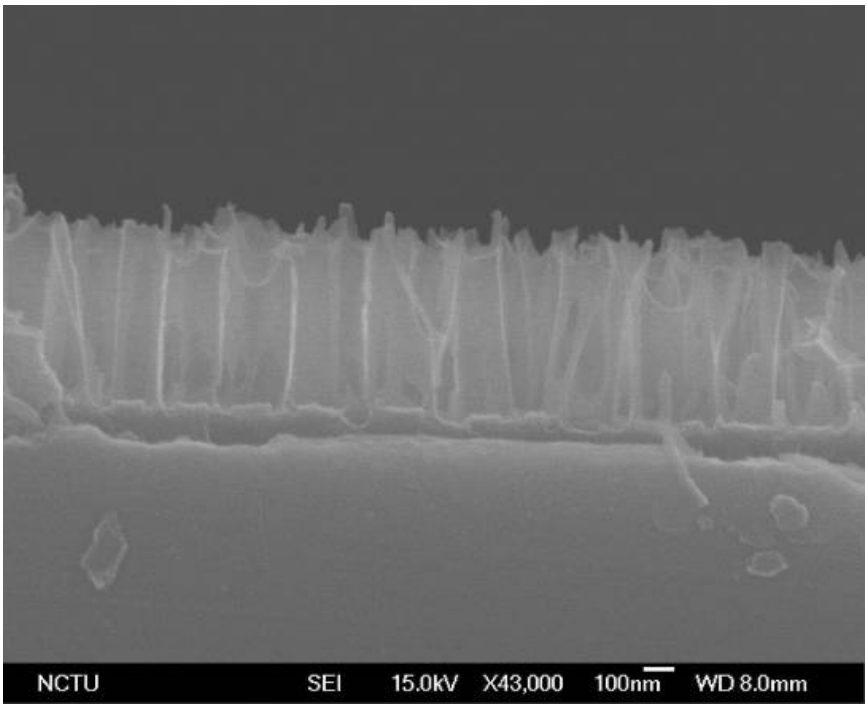

Figure 4-14 Cross-sectional SEM image of TiO_2 nanotube treated by $TiCl_4$ for 10 min and repeated 5 times.

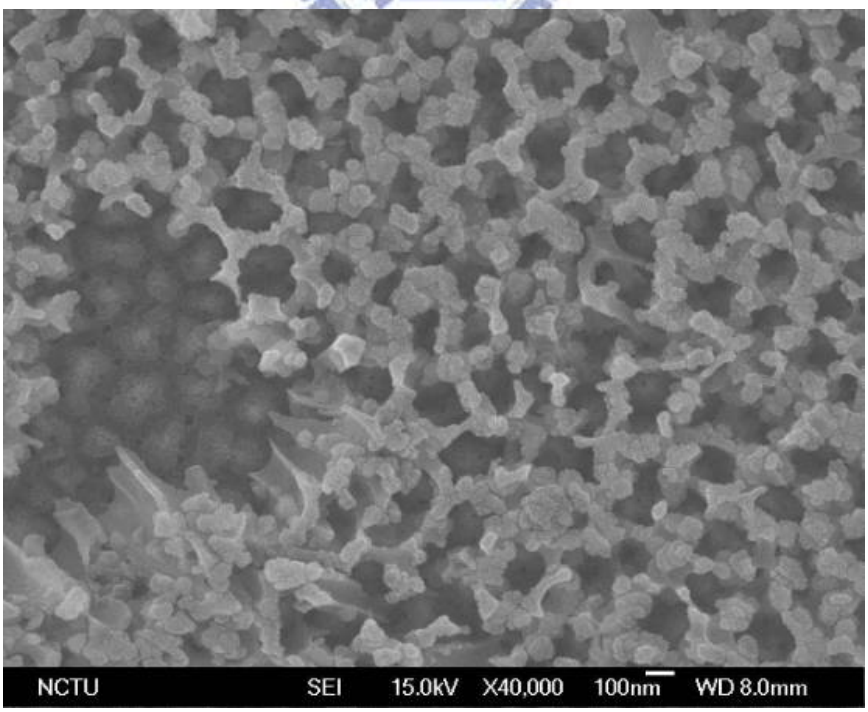

Figure 4-15 Top-view of SEM image of TiO_2 nanotubes after $TiCl_4$ treated.

4.3 Mechanism of Growth of Self-Organized Hollow TiO_2 Hemispheres

Figure 4-16 presents a schematic representation of the mechanism of formation of the hollow hemisphere. In the earlier stage, the upper Al layer was anodized to Al_2O_3, accompanied by the outward migration of Al^{3+} and inward diffusion of O_2^- driven by the applied electric field, leading to the vertical pore channel growth. As the oxide barrier layer at the bottom of the pore approaches the Ti/Al interface, anodization of the underlying titanium can be initiated. The O_2^- migrating inward through the alumina barrier layer is injected into the Ti layer and the titanium oxide nucleus is formed (Figure 4-16 (a)). The growth of the titanium oxide nanostructure resulting from the continuously injecting O_2^- accompanies the volume expansion of titanium oxide formation. In the meanwhile, the barrier layer was thinned by dissolution of H_3PO_4 etching and more O_2^-/OH^- ions passed through it readily. The excess O_2^-/OH^- ions were too many to oxidize these limited Ti ions and combined with themselves. Thus, O_2 gas was released at the anode. The formation of the gaseous oxygen, acting as porogen, producing a great pressure, expand the tantalum oxide hillock and leave a void inside between the hillock and underlying substrate (Figure 4-16 (b)). Note that the barrier under the pore was transferred from a concave into a convex also by the underlying stress. In fact, the similar phenomenon has been observed at the pore bottom of anodized alumina on a silicon substrate without metal interlayer. Although previous reports indicated that these voids may be formed by a localized-temperature-enhanced or electric-field-enhanced dissolution of the alumina near the interface, titanium oxide, an anti-corrosive and thermal-stable material, is dissolved hardly in this condition. This result suggests that the dissolution of the titanium oxide hillock is not the cause of the void formation since physical stress of gaseous pressure has been demonstrated. The anodic current drops and the electrochemical reactions mitigates due to the complete conversion of remaining Al to Al_2O_3. At the end of the anodic oxidation, finally, a hemisphere hollow nanostructure appeared (Figure 4-16 (c)).

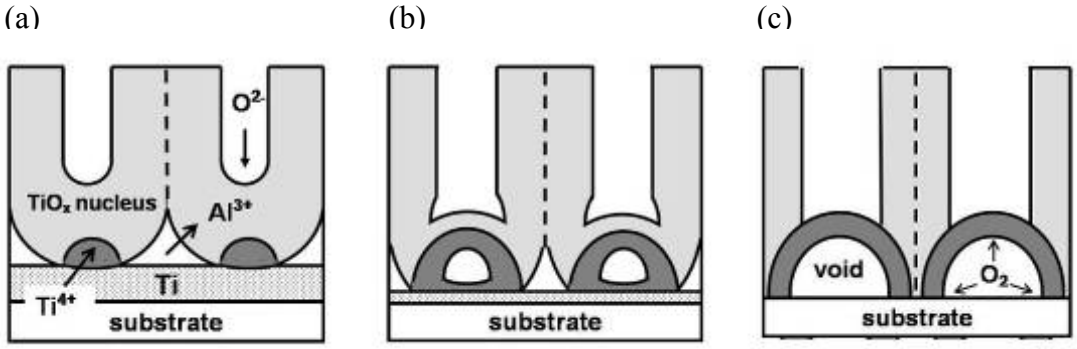

Figure 4-16 Schematic diagrams show the principal steps of modification of the underlying titanium/alumina interface.

4.4 Photoelectric Characterization

4.4.1 I-V Characteristics

In this section we demonstrated effects of electrode film morphologies on the performance of DSSCs by comparing cells based on different working electrode structures, namely, self-organized hollow TiO_2 hemispheres under porous alumina with TiO_2 nanotubes inside and $TiCl_4$ treatment (Sample A), self-organized hollow TiO_2 hemispheres under porous alumina with TiO_2 nanotubes inside (Sample B), TiO_2 film under porous alumina with TiO_2 nanotubes inside (Sample C), self-organized hollow TiO_2 hemispheres under TiO_2 nanotubes (Sample D), and typical TiO_2 nanoparticles (Sample E). Schemes of these electrode structures are shown in Figure 4-17. For Sample B and C, we discussed the effect of hollow TiO_2 hemispheres; for Sample B and D, we verified the role of anodic aluminum oxide in dye-sensitized solar cell; for Sample B and E, we examined the cell performance differences in tube-based and particle-based cells, and for Sample A and B, the influence of $TiCl_4$ treatment has been investigated. The standard back contact used was FTO glass, and the standard counter electrode was platinum-coated FTO glass. A panchromatic sensitizer, N719

dye, was used as the standard dye in the experiments. The standard high boiling point iodide-based electrolyte in 3-methoxypropionitrile (MPN), was employed in this work.

Photovoltaic measurements employed an AM 1.5 solar simulator equipped with a 150 W Xenon lamp, and the power of the simulated light was calibrated to 100 mW/cm^2. The photocurrent (I) and photovoltage (V) of the cell were measured with an active area of 0.25 cm^2.

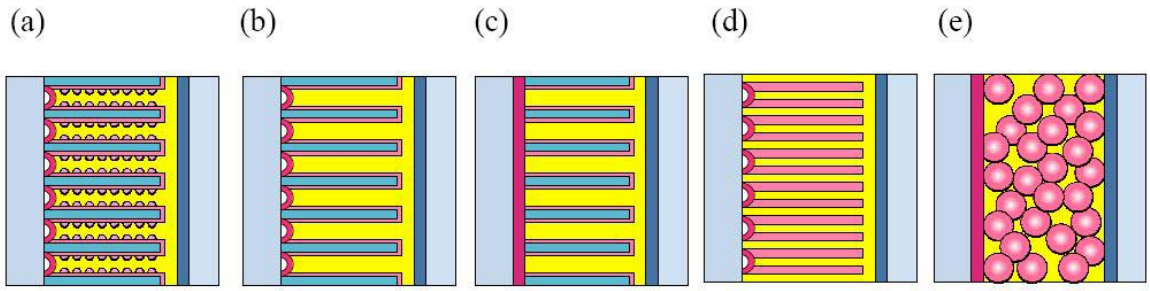

Figure 4-17 Schemes of the electrode structures applied in dye sensitized solar cells (DSSCs) under study. Self-organized hollow TiO_2 hemispheres under porous alumina with TiO_2 nanotubse inside and $TiCl_4$ treatment (a) or not (b), TiO_2 film under porous alumina with TiO_2 nanotubes inside (c), self-organized hollow TiO_2 hemispheres under TiO_2 nanotubes (d), and typical TiO_2 nanoparticles (e).

Representative current-voltage (I-V) measurement and the photovoltaic performance parameters are shown in Figure 4-18 and Table 4-1. For Sample B (self-organized hollow TiO_2 hemispheres under porous alumina with TiO_2 nanotubes inside) with an average titania nanotube diameter of 200 nm and length of 700 nm, the device exhibited an open-circuit voltage (V_{oc}) of 0.59 V, a short-circuit current density (J_{sc}) of 4.66 mA/cm^2, and a fill factor

(FF) of 0.50, giving an overall power conversion efficiency (η) of 1.38%. For Sample C which without self-organized hollow TiO_2 hemispheres, the current density of 4.06 mA/cm^2 and the efficiency of 1.25% were lower than that with self-organized hollow TiO_2 hemispheres (Sample B). Enhanced photoconversion efficiency was obtained due to the predominant role of self-organized hollow TiO_2 hemispheres in promoting electron transport [76] as well as a large surface area for enhanced dye loading [61]. Recent work has revealed that hollow spherical TiO_2 can produce a greatly enhanced photocatalytic activity or photoelectric conversion efficiency due to light multireflections [77, 78]; for the same reason, we believed that the larger J_{SC} value of Sample B is given rise by an enhanced light harvesting due to multiple light reflecting and scattering in-between the hollow hemispherical shells [79] of self-organized hollow TiO_2 hemispheres.

To verify the role of porous alumina in dye-sensitized solar cell, we compared Sample B (with AAO) to Sample D (without AAO) in Table 4-1. Sample B with porous alumina resulted in a 30% improvement in efficiency from 1.06% to 1.38% which demonstrated the porous alumina acted as an insulator barrier between the TiO_2 nanotubes and dye/electrolyte interface [80]. Since the inner TiO_2 nanotubes were shielded by the outer porous alumina from the redox electrolyte, the rate of recombination in this structure (self-organized hollow TiO_2 hemispheres under porous alumina with TiO_2 nanotubes inside) was reduced. Furthermore, clumps and cracklike features in TiO_2 nanotubes have, in fact, been observed. Clusters of bundled TiO_2 nanotubes could be produced during the anodization of titanium, which would slow down electron transport dynamics in electrodes. On the contrary, with the aid of AAO, TiO_2 nanotubes presented without any bundles or microcracks and hence providing electrons a direct pathway toward the FTO glass.

Unlike nanoparticle-based electrode that was randomly arranged and with higher trap density, the nanotube-based electrode provided direct pathways for electron percolation [81]. It can be seen from Table 4-1 that the photocurrent densities of the nanotube-based DSSCs

were larger than that of nanoparticle-based DSSC, which were 4.66 mA/cm^2 of Sample B and 2.59 mA/cm^2 of Sample E. We reasoned that the reduced dimensionality of the nanotube array electrodes, relative to nanoparticulate electrodes, would allow for efficient charge collection due to more rapid electron transport [82, 83]. In addition, the nanoparticles were disordered and were exposed to oxidized species in the liquid electrolyte, which percolated throughout the structure. This enhanced the back reaction and thus led to lower J_{sc} value. Furthermore, the structural disorder at the contact between two nanoparticles leaded to enhanced scattering of free electrons, thus reducing electron mobility [83]. An ordered and strongly interconnected architecture offered the potential for improved electron transport leading to higher photoefficiencies.

It can be seen from Table 4-1 that the most efficient cell, which consisted of self-organized hollow TiO_2 hemispheres under porous alumina with TiO_2 nanotubes inside (Sample B), gave a J_{sc} of 4.66 mA/cm^2, V_{oc} of 0.59 V, and fill factor of 0.50, yielding an overall conversion efficiency of 1.38%. While there were essentially no substantial differences in the photovoltages, the structure exhibited a 1.1 times improvement compared to the second efficient cell (Sample C). Dye sensitized solar cells which the working electrodes were moulded in self-organized hollow TiO_2 hemispheres exhibited more photocurrent than equivalent reference cells with no such structure at all.

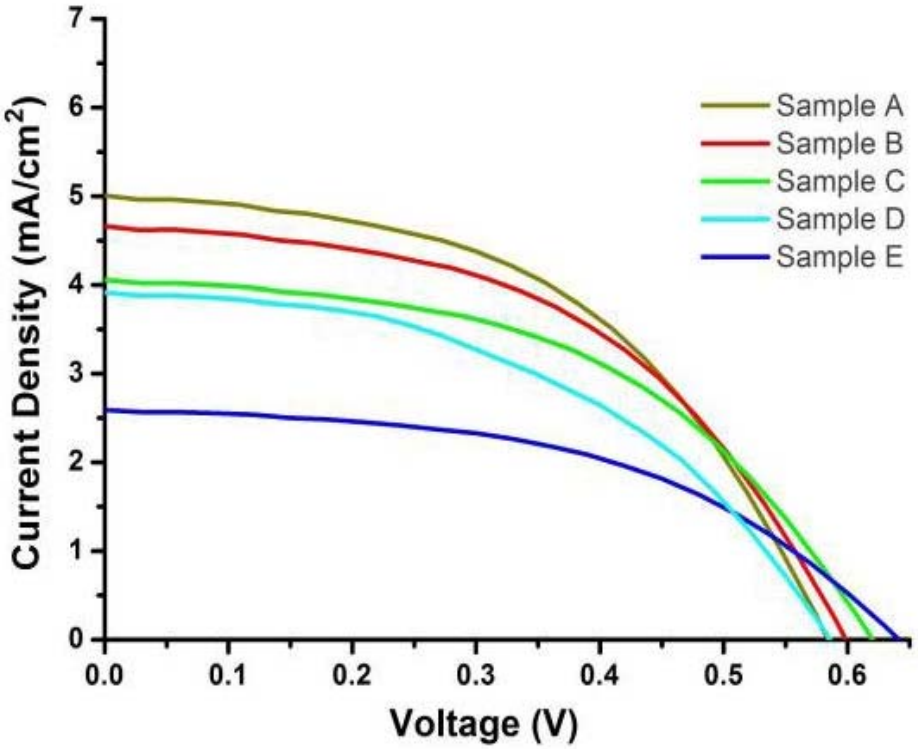

Figure 4-18 Photocurrent density-voltage characteristics of the DSSCs using: self-organized hollow TiO_2 hemispheres under porous alumina with TiO_2 nanotubes inside treated by $TiCl_4$ (Sample A, the brown one), self-organized hollow TiO_2 hemispheres under porous alumina with TiO_2 nanotubes inside (Sample B, the red one), TiO_2 film under porous alumina with TiO_2 nanotubes inside (Sample C, the green one), self-organized hollow TiO_2 hemispheres under TiO_2 nanotubes (Sample D, the light blue one), and typical TiO_2 nanoparticles (Sample E, the dark blue one).

Devices	J_{sc} (mA/cm^2)	V_{oc} (V)	FF (%)	η (%)
Sample A	5.00	0.58	58	1.45
Sample B	4.66	0.59	50	1.38
Sample C	4.06	0.62	59	1.25
Sample D	3.91	0.58	46	1.06
Sample E	2.59	0.64	49	0.82

Table 4-1 Summary of the dye-sensitized solar cell performance metrics for cells constructed with various TiO_2 morphologies as electrodes: self-organized hollow TiO_2 hemispheres under porous alumina with TiO_2 nanotubes inside treated by $TiCl_4$ (Sample A), self-organized hollow TiO_2 hemispheres under porous alumina with TiO_2 nanotubes inside (Sample B), TiO_2 film under porous alumina with TiO_2 nanotubes inside (Sample C), self-organized hollow TiO_2 hemispheres under TiO_2 nanotubes (Sample D), and typical TiO_2 nanoparticles (Sample E).

4.4.2 $TiCl_4$ Processed DSSC

With sufficient understanding of the effects of electrode morphology, it is meaningful to discover the influences of the post treatment. Treatment of titanium tetrachloride solution on TiO_2 nano-crystal has been confirmed to be able to improve the conversion efficiency of DSSC in previous works [64, 74, 84]. The effect of the post-treatment on TiO_2 nanotubes morphology was characterized by SEM and demonstrated that $TiCl_4$ treatment made the surface of the TiO_2 nanotubes much rougher when compared to that of untreated ones as Figure 4-12 showed. Special attention was given in this study to further confirm the influence of post-treatment on DSSC performance.

Figure 4-19 (a) shows the current-voltage (I-V) measurement corresponding to the electrode comprised self-organized hollow TiO_2 hemispheres under porous alumina with TiO_2 nanotubes inside treated by $TiCl_4$ (Sample A). The device with an average titania nanotube diameter of 200 nm and length of 700 nm exhibited an open-circuit voltage (V_{oc}) of 0.58 V, a short-circuit current density (J_{sc}) of 5.00 mA/cm^2, and a fill factor (FF) of 0.48, giving an overall power conversion efficiency (η) of 1.45%. In comparison to the untreated-DSSC (Sample B), Sample A exhibited superior current density. It can be attributed to the $TiCl_4$ treatment further enlarging their surface areas by creating lots of TiO_2 nanoparticles on nanotubes, thus leading to a higher adsorption of the dye and an improved photogenerated current in the DSSC. We also noted that the efficiency of Sample A is 1.1 times the efficiency of non-$TiCl_4$-treated cells; we hypothesized that the $TiCl_4$ treatment facilitated improved bonding between the TiO_2 and dye molecule, resulting in improved charge transfer. In conclusion, the $TiCl_4$ post-treatment, in addition to providing extra TiO_2 surface area, has been proven to also enhance the light absorption and dye adsorption of the anode, benefiting the performance of dye-sensitized solar cell.

(a)

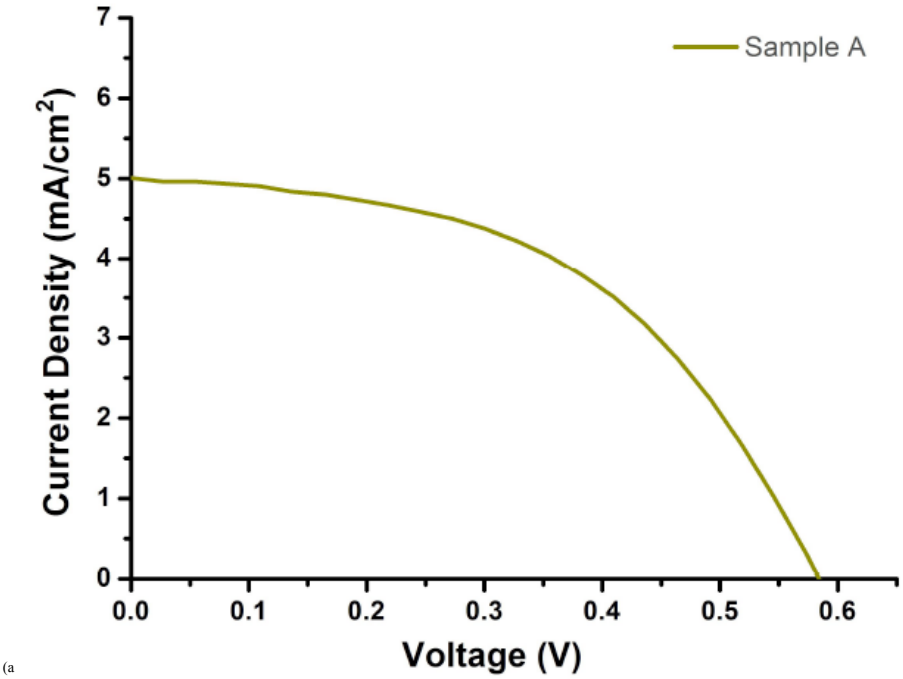

(a

(b)

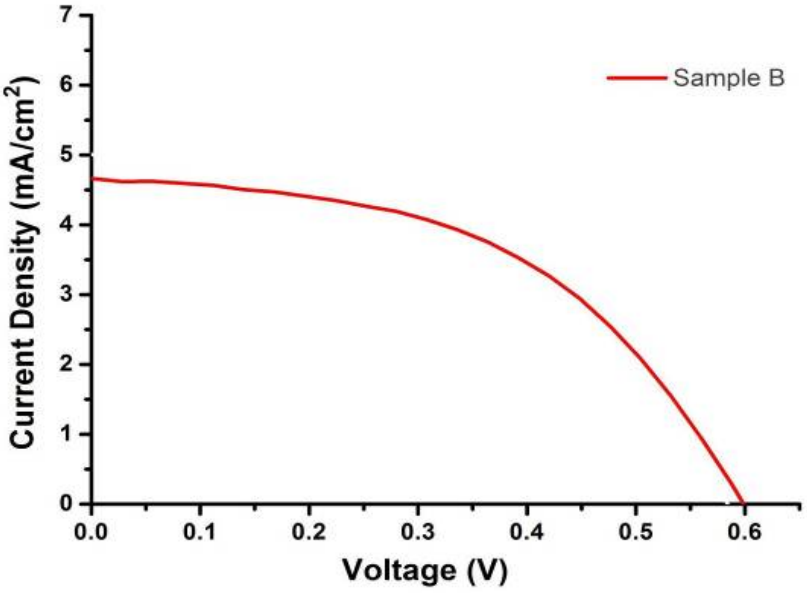

Figure 4-19 Photocurrent density-voltage characteristics of the DSSCs. (a) Self-organized hollow TiO_2 hemispheres under porous alumina with TiO_2 nanotubes inside treated by $TiCl_4$ (Sample A). (b) Self-organized hollow TiO_2 hemispheres under porous alumina with TiO_2 nanotubes inside without $TiCl_4$ treated (Sample B).

Chapter 5: Conclusions

We have successfully fabricated self-organized hollow TiO_2 hemispheres under porous anodic aluminum oxide (AAO) with TiO_2 nanotubes inside directly on FTO glass and used them as working electrodes in dye-sensitized solar cells. By depositing a thin layer of Ti on FTO substrates before anodization, we not only form self-organized hollow TiO_2 hemispheres, but also improve the contact between FTO substrates and overlaying aluminum. This more stable AAO on FTO substrates is highly suitable for the subsequent TiO_2 isopropoxide sol-gel process.

The novel structure combines TiO_2 materials of 0-D hemispheres, 1-D nanotubes, and 2-D films which benefits by their characteristics of large contact area, direct electron transport path, and massive dye absorption, respectively. The unique morphology provided a photocurrent magnitude of 5.00 mA/cm^2 and an open circuit voltages of 0.58 V under air mass 1.5 illumination from a 700-nm-thick nanotube array. The relatively short nanotube array results in considerably less photoabsorption than, for example, the current DSSC gold-standard of a 10-μm-thick layer of TiO_2 nanoparticles. It is believed that by increasing the length of nanotube array on the electrode, we could possibly improve efficiencies of dye-sensitized solar cells. Current challenge is to produce TiO_2 nanotubes within porous anodic alumina of micrometer length.

In summary, the electrode of self-organized hollow TiO_2 hemispheres under porous anodic alumina with TiO_2 nanotubes inside was successfully prepared via modified anodization and sol-gel infiltration in room temperature. The synthesis method is simple, of low cost, and highly reproducible. It suggests that the novel architecture to be a very promising electrode.

Reference

1. P. V. Kamat, J. Phys. Chem. C **111**, 2834 (2007)
2. C. D. Keeling, T. P. Whorf, M. Wahlen, J. Vanderplicht, Nature **375**, 666 (1995)
3. G. W. Crabtree, N. S. Lewis, Phys. Today **60**, 37 (2007)
4. M. Gratzel, Inorg. Chem. **44**, 6841 (2005)
5. R. E. H. Sims, MRS Bull. **33**, 389 (2008)
6. K. W. J. Barnham, M. Mazzer, B. Clive, Nat. Mater. **5**, 161 (2006)
7. U. Bach, D. Lupo, P. Comte, J. E. Moser, F. Weissortel, J. Salbeck, H. Spreitzer, M. Gratzel, Nature **395**, 583 (1998)
8. B. O'Regan, M. Gratzel, Nature **353**, 737 (1991)
9. G. Yu, J. Gao, J. C. Hummelen, F. Wudl, A. J. Heeger, Science **270**, 1789 (1995)
10. J. van de Lagemaat, T. M. Barnes, G. Rumbles, S. E. Shaheen, T. J. Coutts, C. Weeks, I. Levitsky, J. Peltola, P. Glatkowski, Appl. Phys. Lett. **88**, 233 (2006)
11. M. Zukalova, A. Zukal, L. Kavan, M. K. Nazeeruddin, P. Liska, M. Gratzel, Nano Lett. **5**, 1789 (2005)
12. M. Adachi, Y. Murata, J. Takao, J.T. Jiu, M. Sakamoto, F.M. Wang, J. Am. Chem. Soc. **126**, 14943 (2004)
13. M. Law, L. E. Greene, J. C. Johnson, R. Saykally, P. D. Yang, Nat. Mater. **4**, 455 (2005)
14. K. Zhu, N.R. Neale, A. Miedaner, A.J. Frank, Nano Lett. **7**, 69 (2007)
15. S. Funk, B. Hokkanen, U. Burghaus, A. Ghicov, P. Schmuki, Nano Lett. **7**, 1091 (2007)
16. C. M. Ruan, M. Paulose, O. K. Varghese, G. K. Mor, C. A. Grimes, J. Phys. Chem. B **109**, 15754 (2005)
17. J. M. Macak, H. Tsuchiya, P. Schmuki, Angew. Chem. Int. Ed. **44**, 2100 (2005)

18. J. M. Macak, H. Tsuchiya, L. Taveira, S. Aldabergerova, P. Schmuki, Angew. Chem. Int. Ed. **44**, 7463 (2005)

19. M. Paulose, K. Shankar, O. K. Varghese, G. K. Mor, B. Hardin, C. A. Grimes, Nanotechnology **17**, 1446 (2006)

20. G. K. Mor, K. Shankar, M. Paulose, O. K. Varghese, C. A. Grimes, Nano Lett. **6**, 215 (2006)

21. S. P. Albu, A. Ghicov, J. M. Macak, R. Hahn, P. Schmuki, Nano Lett. **7**, 1286 (2007)

22. J. Park, S. Bauer, K. von der Mark, P. Schmuki, Nano Lett. **7**, 1686 (2007)

23. H. J. Fan, P. Werner, M. Zacharias, Small **2**, 700 (2006)

24. I. Lombardi, A. I. Hochbaum, P. D. Yang, C. Carraro, R. Maboudian, Chem. Mater. **18**, 988 (2006)

25. H. Gerischer, M. Lubke, J. Electroanal. Chem. **204**, 225 (1986)

26. R. Vogel, K. Pohl, H. Weller, Chem. Phys. Lett. **174**, 241 (1990)

27. S. Kohtani, A. Kudo, T. Sakata, Chem. Phys. Lett. **206**, 166 (1993)

28. R. Vogel, P. Hoyer, H. Weller, J. Phys. Chem. **98**, 3183 (1994)

29. R. Plass, S. Pelet, J. Krueger, M. Gratzel, U. Bach, J. Phys. Chem. B **106**, 7578 (2002)

30. L. M. Peter, K. G. U. Wijayantha, D. J. Riley, J. P. Waggett, J. Phys. Chem. B **107**, 8378 (2003)

31. D. Liu, P. V. Kamat, J. Phys. Chem. **97**, 10769 (1993)

32. A. Zaban, O. I. Micic, B. A. Gregg, A. J. Nozik, Langmuir **14**, 3153 (1998)

33. H. Gerischer, Photo. Chem. Bio. **16,** 243 (1972)

34. A. Hagfeldt, M. Gratzel, Chem. Res. **33**, 269 (2000)

35. B. Oregan, M. Gratzel, Nature **353**, 737 (1991)

36. D. Cahen, G. Hodes, M. Gratzel, J. F. Guillemoles, I. Riess, J. Phys. Chem. B **104**, 2053 (2000)

37. S. A. Haque, Y. Tachibana, R. L. Willis, J. E. Moser, M. Gratzel, D. R. Klug, J. R.

Durrant, J. Phy. Chem. B **104**, 538 (2000)

38. A. M. Ferrenberg, R. H. Swendsen, Phys. Rev. Lett. **61**, 2635 (1988)
39. P. Wang, S. M. Zakeeruddin, J. E. Moser, M. K. Nazeeruddin, T. Sekiguchi, M. Gratzel, Nat. Mater. **2**, 402 (2003)
40. K. Hara, M. Kurashigo, Y. Dan-oh, C. Kasasa, Y. Ohga, A. Shinpo, S. Suga, K. Sayama, H. Arakawa, New. J. Chem. **27**, 783 (2003)
41. T. Horiuchi, H. Miura, K. Sumioka, S. Uchida, J. Am. Chem. Soc. **126**, 12218 (2004)
42. N. Vlachopoulos, P. Liska, J. Augustynski, M. Gratzel, J. Am. Chem. Soc **110**, 1216 (1988)
43. C. J. Barbe, F. Arendse, P. Comte, M. Jirousek, F. Lenzmann, V. Shklover, M. Grazel, J. Am. Ceram. Soc. **80**, 3157 (1997)
44. A. Hagfeldt, M. Grätzel, Chem. Rev. **95**, 49 (1995)
45. L. E. Greene, M. Law, J. Goldberger, F. Kim, J. C. Johnson, Y. Zhang, R. J. Saykally, P. Yang, Angew. Chem. Int. Ed. Engl. **42**, 3031 (2003)
46. B. Kim, W. M. Sigmund, Langmuir **20**, 8239 (2004)
47. Y. C. Xing, J. Phys. Chem. B **108**, 19255 (2004)
48. I. Robel, B. A. Bunker, P. V. Kamat, Adv. Mater. **17**, 2458 (2005)
49. E. Hendry, M. Koeberg, B. O'Regan, M. Bonn, Nano. Lett. **6**, 755 (2006)
50. F. Y. Oliva, L. B. Avalle, E. Santos, O. R. Camara, J. Photochem. Photobiol. **146**, 175 (2002)
51. R. Tenne, C.N.R. Rao, Philos. Trans. R. Soc. A **362**, 2099 (2004)
52. M. Gratzel, J. Photochem. Photobiol. A **168**, 235 (2004)
53. M. Law, L.E. Greene, J.C. Johnson, R. Saykally, P.D. Yang, Nat. Mater. **4**, 455 (2005)
54. M. Adachi, Y. Murata, I. Okada, S. Yoshikawa, J. Electrochem. Soc. **150**, 488 (2003).
55. K. M. Gopal, S. Karthik, P. Maggie, K. V. Oomman, Nano Lett. **6**, 215 (2006)
56. F. Fabregat, J. Garcia. E. Palomares, J.N. Clifford, S. A. Haque, J. R. Durrant, J. Bisquert,

J. Appl. Phys. **96**, 6903 (2004)

57. Z. Kai, B. V. Todd, R. N. Nathan, J. F. Arthur Nano Lett. **7**, 3739 (2007)
58. S. J. Limmer, S. Seraji, Y. Wu, T. P. Chou, C. Nguyen, G. Z. Cao, Adv. Mater. **13**, 1269 (2001)
59. S. J. Limmer, T. P. Chou, G. Z. Cao, J. Mater. Sci. **39**, 895 (2004)
60. S. Liu, K. Huang, Sol. Energy Mater. Sol. Cells **85**, 125 (2005)
61. S. Z. Chu, K. Wada, S. Inoue, S. Todoroki, Chem. Mater. **14**, 266 (2003)
62. A. B. Martinson, J. W. Elam, J. T. Hupp, M. J. Pellin, Nano Lett. **7**, 2183 (2007)
63. A. B. Martinson, J. W. Elam, J. Liu, M. J. Pellin, T. J. Marks, J. T. Hupp, Nano Lett. **8**, 2862 (2008)
64. S. C. Yang, D. J. Yang, J. Kim, J. M. Hong, H. G. Kim, I. D. Kim, H. Lee, Adv. Mater. **20**, 1059 (2008)
65. S. I. Matsushita, N. Fukuda, M. Shimomura, Colloids Surf. A **15**, 257, (2005)
66. M. Adachi, Y. Murata, M. Harada, Y. Yoshikawa, Chem. Lett. **29**, 942 (2000)
67. O. K. Varghese, D. Gong, M. Paulose, K. G. Ong, E. C. Dickey, C. A. Grimes, Adv. Mater. **15**, 624 (2003)
68. G. K. Mor, K. Shankar, O. K. Varghese, C. A. Grimes, J. Mater. Res. **19**, 2989 (2004)
69. T. S. Kang, A. P. Smith, B. E. Taylor, M. F. Durstock, Nano Lett. **9**, 601 (2009)
70. M. Adachi, Y. Murata, J. Takao, J. Jiu, M. Sakamoto, F. Wang, J. Am. Chem. Soc. **126**, 14943 (2004)
71. D. Zhang, T. Yoshida, T. Oekermann, Adv. Mater. **16**, 1228 (2006)
72. R. Scotti, I. R. Bellobono, C. Canevali, C. Cannas, M. Catti, M. D'Arienzo, Chem. Mater. **20**, 4051 (2008)
73. G. K. Mor, O. K. Varghese, M. Paulose, K. Shankar, C. A. Grimes, Sol. Energy Mater. Solar Cells **90**, 2011 (2006)
74. K. Zhu, T. B. Vinzant, N. R. Neale, A. J. Frank, Nano Lett. **7**, 12 (2007)

75. N. G. Park, G. Schlichthorl, J. van de Lagemaat, H. M. Cheong, A. Mascarenhas, A. J. Frank, J. Phys. Chem. B **17**, 3308 (1999)

76. S. I. Matsushita, N. Fukuda, M. Shimomura, Colloids Surf. A **15**, 257 (2005)

77. H. Li, Z. Bian, J. Zhu, D. Zhang, G. Li, Y. Huo, H. Li, Y. Lu, J. Am. Chem. Soc. **129**, 8406 (2007)

78. J. H. Pan, X. Zhang, A. J. Du, D. D. Sun, J. O. Leckie, J. Am. Chem. Soc. **130**, 11256 (2008)

79. F. Luo, L. Wang, B. Ma, Y. Qiu, J. Photochem. Photobiol. A: Chem. **197**, 375 (2008)

80. J. E. Boercker, E. E. Pommer, E. S. Aydi, Nanotechnology **19**, 095604 (2008)

81. E. Galoppini, J. Rochford, H. Chen, G. Saraf, Y. Lu, A. Hagfeldt, G. Boschloo, J. Phys. Chem. B **110**, 16159 (2006)

82. A. B. F. Martinson, J. E. McGarrah, M. O. K. Parpia, J. T. Hupp, Phys. Chem. Chem. Phys. **8**, 4655 (2008)

83. T. Y. Peng, A. Hasegawa, J. R. Qiu, K. Hirao, Chem. Mater. **15**, 2011 (2003)

84. M. Y. Song, D. K. Kim, S. M. Jo, D. Y. Kim, Syn. Met. **155**, 635 (2005)